Structural Complexity and Mechanics of a Shallow Crustal Seismogenic Source (Vado di Corno Fault Zone, Italy)

M. Fondriest, F. Balsamo, A. Bistacchi, L. Clemenzi, M. Demurtas, F. Storti, G. Di Toro

JGR Solid Earth

RESEARCH ARTICLE
10.1029/2019JB018926

Structural Complexity and Mechanics of a Shallow Crustal Seismogenic Source (Vado di Corno Fault Zone, Italy)

M. Fondriest[1,2,3], F. Balsamo[4], A. Bistacchi[5], L. Clemenzi[4], M. Demurtas[6], F. Storti[4], and G. Di Toro[2,7]

[1]Institut des Sciences de la Terre (ISTerre), Universitè Grenoble Alpes, Grenoble, France, [2]Dipartimento di Geoscienze, Università degli Studi di Padova, Padua, Italy, [3]Department of Earth and Environmental Sciences (DEES), University of Manchester, Manchester, UK, [4]NEXT, Università degli Studi di Parma, Parma, Italy, [5]Università degli Studi di Milano-Bicocca, Milan, Italy, [6]The Njord Centre, University of Oslo, Oslo, Norway, [7]Istituto Nazionale di Geofisica e Vulcanologia (INGV), Rome, Italy

Key Points:
- High-resolution mapping and 3-D fault network modeling depict the complex internal structure of an extensional seismogenic fault zone
- The segmentation and slip distribution of the extensional fault zone are controlled by the geometry of a preexisting thrust zone
- Structural inheritance and mechanical stratigraphy play a first-order control on the mechanics and seismogenic behavior of the extensional fault zone

Supporting Information:
- Supporting Information S1

Correspondence to:
M. Fondriest,
michelefondriest@yahoo.it;
michele.fondriest@univ-grenoble-alpes.fr

Citation:
Fondriest, M., Balsamo, F., Bistacchi, A., Clemenzi, L., Demurtas, M., Storti, F., & Di Toro, G. (2020). Structural complexity and mechanics of a shallow crustal seismogenic source (Vado di Corno Fault Zone, Italy). *Journal of Geophysical Research: Solid Earth*, *125*, e2019JB018926. https://doi.org/10.1029/2019JB018926

Received 22 OCT 2019
Accepted 10 AUG 2020
Accepted article online 11 AUG 2020

Author Contributions:
Data curation: M. Fondriest, F. Balsamo, A. Bistacchi, L. Clemenzi, M. Demurtas, F. Storti, G. Di Toro
Formal analysis: M. Fondriest
Investigation: M. Fondriest, F. Balsamo, A. Bistacchi, L. Clemenzi, M. Demurtas, F. Storti, G. Di Toro
Methodology: M. Fondriest, A. Bistacchi
Writing - original draft: M. Fondriest
Writing – review & editing: M. Fondriest, F. Balsamo, A. Bistacchi, L. Clemenzi, M. Demurtas, F. Storti, G. Di Toro

Abstract The mechanics and seismogenic behavior of fault zones are strongly influenced by their internal structure. In this perspective, the internal structure of the extensional seismically active Vado di Corno Fault Zone (VCFZ, Central Apennines, Italy) was quantified by combining high-resolution structural mapping with 3-D fault network analysis over ~2 km along fault strike. The fault zone was exhumed from ~2 km depth in carbonate rocks, accommodated 1.5–2 km of extensional throw since Early Pleistocene, and cuts through the Pliocene Omo Morto Thrust Zone (OMTZ) with partial reactivation in extension. The exceptional exposure of the footwall block allowed us to reconstruct in detail the geometry of the OMTZ and quantify the spatial arrangement of master/subsidiary faults and fault zone rocks within the extensional VCFZ. The combination of the structural map and the 3-D fault network with kinematic and topological analyses pointed out the crucial role of the older thrust geometry (i.e., lateral ramps) in controlling the along-strike segmentation and slip distribution of the VCFZ. These observations were discussed in the framework of regional extension through a slip tendency analysis and a simplified mechanical model, which suggest the activation of oblique inherited structures during the lateral propagation of the VCFZ segments. The interaction of the VCFZ with the OMTZ generated along strike and possibly downdip mechanical asperities. Considering the exhumed VCFZ as an analog for the shallow structure of other seismic sources in the Central Apennines, similar settings could play first-order control on the spatio-temporal evolution and rupture heterogeneity of earthquakes in the region.

1. Introduction

Brittle fault zones are volumes of variably deformed rocks (i.e., fault rocks and fractured rock masses) characterized by distinct elastic, frictional, and transport properties compared to the surrounding wall rocks, which impart them specific mechanical, hydrological, and seismogenic behaviors (Caine et al., 1996; Chester et al., 1993; Faulkner et al., 2003; Wibberley et al., 2008). The internal structure of fault zones is described in three dimensions by the spatial distribution of fault zone rocks and subsidiary faults and fractures. Since the seminal work of Caine et al. (1996), a three-component structural architecture template, including fault core, damage zone, and host rock, has been widely applied to describe brittle fault zones (Wibberley et al., 2008). The fault core represents the structural unit where most of the displacement is accommodated and typically consists of high-strain and low-permeability fault rocks (e.g., gouges, cataclasites, and breccias), whereas the damage zone is a lower-strain unit affected by subsidiary faulting and fracturing leading to a relative bulk permeability increase (Caine et al., 1996; Faulkner et al., 2010; Storti et al., 2003). Although this scheme can be a useful first-order tool to describe the permeability structure and the expected fluid regime within fault zones, it is much less informative about their geometry, topology and mechanics.

Direct characterization of the internal structure of brittle fault zones in the subsurface is limited to sparse borehole data, while seismic and other geophysical methods (e.g., tomography based on different observables) can provide high-quality 2-D or 3-D characterizations but still affected by noise and resolution limits (e.g., Amoroso et al., 2017; Ben-Zion, 1998; Cochran et al., 2009; Hale, 2013; Iacopini et al., 2016; Pischiutta et al., 2017; Vidale & Li, 2003). In the case of seismogenic fault zones, modern techniques of

aftershock relocation (i.e., double difference method and earthquake detection algorithms with deep neural networks) allowed seismologists to illuminate with unprecedented internal spatial resolution (~10 m of relocation precision for correlated events) the three-dimensional fault networks activated during seismic sequences (Chiaraluce et al., 2011; Ross et al., 2020; Valoroso et al., 2013). Such studies indicate that earthquake faulting is complex in space and time, with geometrical and kinematic irregularities often related to coseismic slip or rupture velocity variability at the seismic source scale (Cirella et al., 2012; Di Stefano et al., 2011).

The study of natural exposures of exhumed fault zones remains the best tool to characterize their internal structure at scales relevant to seismic rupture dynamics and to directly assess the effect of inherited anisotropies on fault zones nucleation and growth (Rowe & Griffith, 2015; Wibberley et al., 2008). Microstructural and mineralogical characterization of fault rocks gives the chance to investigate the deformation (i.e., mechanical, chemical, and hydraulic) processes that were active through fault zone lifetimes (e.g., Clemenzi et al., 2015; Di Toro & Pennacchioni, 2005; Fagereng & Sibson, 2010; Fondriest et al., 2012; Leah et al., 2018; Masoch et al., 2019; Sibson, 1986; Smith et al., 2011; Snoke et al., 1998; Tesei et al., 2013). However, most field studies characterize the local internal structure of fault zones based on the description of limited across-strike fault zone exposures and lack information about along-strike and downdip fault architecture variability, including fault geometry and kinematics. One way to overcome these limits is to study exhumed fault zones characterized by an excellent preservation of the fault/fracture networks across extensive and laterally continuous exposures (at least few kilometers along strike), where it is possible to perform high-resolution fault zone mapping and apply modern techniques of fault network analysis and modeling in three dimensions. To our knowledge, only a few field studies adopt a similar approach (e.g., Balsamo et al., 2016; Bistacchi et al., 2010; Delogkos et al., 2020; Smith et al., 2013; Swanson, 1988), and only Faulkner et al. (2003) mapped with significant detail the internal structure of a major strike-slip fault zone (the Carboneras Fault Zone) for a length of a few kilometers.

In this study, we quantified the internal structure of a ~2 km long segment of the Vado di Corno Fault Zone (VCFZ), an extensional seismically active fault zone cutting through carbonate host rocks in the Central Apennines of Italy. The work builds on a previous study by Demurtas et al. (2016), where a single cross section of the VCFZ was described, including both the fault core and the footwall damage zone, pointing out the occurrence of an inherited thrust fault zone (Omo Morto Thrust Zone, OMTZ), which was cut and partially inverted by Quaternary extensional faulting. This geometry resembles that illuminated in the subsurface by the L'Aquila 2009 seismic sequence, which occurred few kilometers to the southwest (Demurtas et al., 2016; Valoroso et al., 2013). Potential evidence for past seismic faulting in the exhumed fault rocks were suggested by the combination of peculiar features such as intense volumetric deformation (i.e., in situ shattering sensu Fondriest et al., 2015, 2017) and extreme shear strain localization (i.e., mirror-like fault surfaces with truncated clasts, highly localized sheared calcite veins, and fluidized ultracataclasites) within the fault core. All these observations support interpreting the VCFZ as an exhumed analog of the shallow crustal portion of seismogenic sources producing moderate to large in magnitude earthquakes in the Central Apennines of Italy (Demurtas et al., 2016).

We present here a high-resolution structural map (mapped at 1:500 scale) of the VCFZ footwall block over an area of ~1 km^2, which pictures the topology of both master and subsidiary fault surfaces and the spatial arrangement of fault and host rocks. A 3-D fault network model was then reconstructed from the map, integrating structural data collected on the surface such as (i) fault surface geometry and topology, (ii) fault kinematics, and (iii) fault rock distribution. The combination of the structural map and the 3-D fault network analysis allowed us to (i) determine the thickness and spatial relations of the different fault rock units, (ii) reconstruct the three-dimensional geometry of the older thrust zone (OMTZ), (iii) analyze the 3-D kinematic framework of the whole fault zone, and (iv) quantify the topology of the fault network. As a relevant outcome we demonstrate how the original and articulated geometry of the inherited OMTZ (i.e., frontal and lateral ramps) strongly influenced the along-strike segmentation and kinematics of the newly formed extensional VCFZ. We finally discuss the origin of these geometrical and kinematic complexities in the context of regional active extension by coupling a slip tendency analysis and a boundary element method (BEM) fault elastic model.

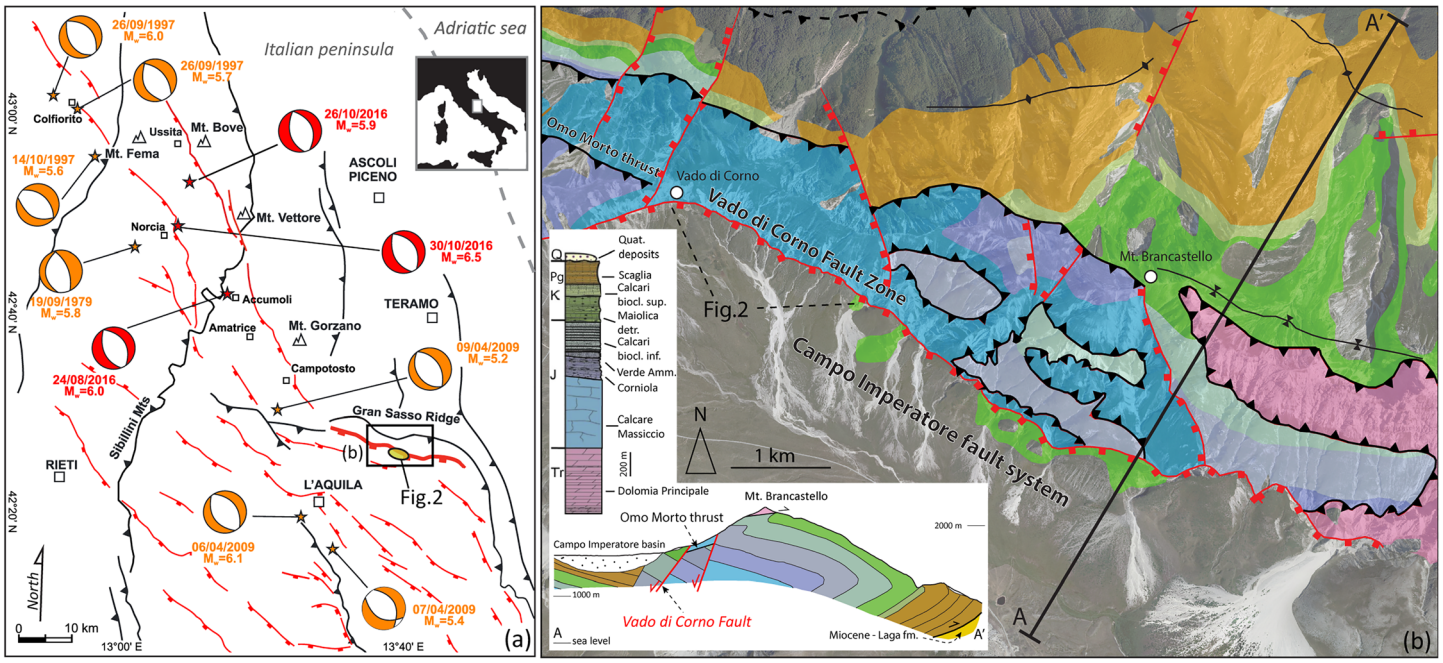

Figure 1. Geological setting. (a) Seismotectonic map covering the northern portion of the Central Apennines and the southern portion of the Northern Apennines of Italy (modified after Pizzi et al., 2017). Main thrust faults are in black, and Quaternary active extensional faults are in red. The thicker red line indicates the Campo Imperatore Fault system (CIFS), part of which is investigated in this study. Focal mechanisms indicate the mainshocks of the seismic sequences which stroke the region in the last 40 years (in red the mainshocks of the 2016 seismic sequence, in orange all the others). (b) Geological map and cross section of the Campo Imperatore area (modified after Demurtas et al., 2016; simplified from the published Foglio 349 "Gran Sasso d'Italia"; Ispra, 2012); see inset in Section (a) for location. Thrust faults are in black, and active extensional faults are in red. The CIFS borders the Campo Imperatore intermountain basin to the north and runs from Vado di Corno along the base of Mt. Brancastello with an WNW-ESE strike. In this study, we focused on the Vado di Corno Fault Zone (VCFZ) segment and its interaction with the older OMTZ (see also Section A-A′).

2. Geological and Seismotectonic Setting

The study area is located in the Central Apennines of Italy, a ENE verging fold and thrust belt developed in Cenozoic times due to the collision between the Adria and European plates (e.g., Elter et al., 1975; Jolivet et al., 1998) (Figure 1a). Since Miocene times, the eastward migration of the outer deformation front was associated with back-arc extension to the west, in the European plate, because of the Adria plate subduction rollback (Jolivet & Faccenna, 2000; Malinverno & Ryan, 1986). This caused a widespread orogen-perpendicular NE-SW extension within the Apenninic belt, accommodated by orogen-parallel Quaternary extensional fault systems (e.g., Ghisetti & Vezzani, 1991; Patacca et al., 1990). Many of these fault systems are active seismogenic structures, modulating the extension of the area (extension rates of ~3 mm/year based on GPS measurements; Serpelloni et al., 2005; D'Agostino et al., 2008), which are responsible for several destructive earthquake sequences that struck the region both historically and in the last few years (e.g., Chiarabba et al., 2009; Chiaraluce et al., 2017) (Figure 1a).

The upper crust of the Central Apennines is characterized by a carbonate-dominated succession with thickness up to 8–10 km (Patacca et al., 2008; Speranza & Minelli, 2014). This thick carbonate layer derives from the piling up of thrust sheets during compression and also reflects primary thickness variations inherited from the Upper Triassic to Middle Jurassic syntectonic sedimentation in an extending passive margin (Boccaletti et al., 1971; Patacca et al., 1990). The facies distribution, controlled by the original paleogeography, resulted in mechanical heterogeneities that strongly influenced both the evolution of the fold and thrust belt, and the development of the younger extensional structures (Santantonio & Carminati, 2011; Speranza & Minelli, 2014; Speranza et al., 2003; Vezzani et al., 2010). Although several authors have proposed different kinematic scenarios for the structural framework of the Central Apennines at the regional scale (e.g., out of sequence thrusting, rotation of inherited extensional faults, and postorogenic extensional collapse; Calamita et al., 2003; Cardello & Doglioni, 2014; D'Agostino et al., 1998; Ghisetti & Vezzani, 1991; Storti et al., 2018),

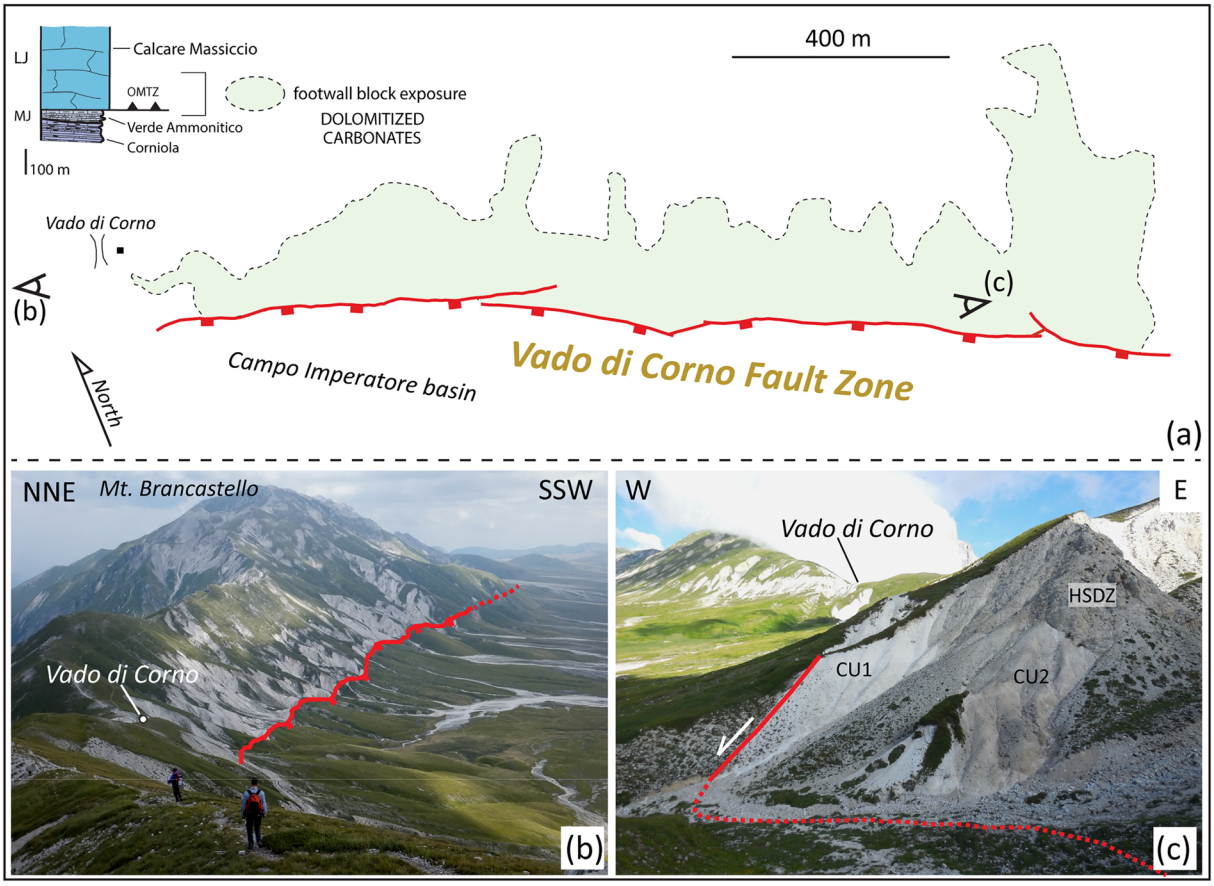

Figure 2. The Vado di Corno Fault Zone (VCFZ). (a) Map view of the VCFZ footwall block exposure in Campo Imperatore. Tectonostratigraphic scheme (top left corner) of the VCFZ footwall block: *Calcare Massiccio Fm.* (Lower Jurassic) is thrusted over *Verde Ammonitico Fm.* (Middle Jurassic) (see stratigraphy in Figure 1 for total thicknesses of the formations). The fault zone is wonderfully exposed with an exceptional lateral continuity for ~2 km along fault strike and up to ~400 m across fault strike. Viewpoints of Sections (b) and (c) are reported in the map. (b) View from the eastern slope of Mt. Aquila toward the VCFZ, whose footwall is extensively outcropping within a series of badlands. (c) Natural section through the VCFZ. The master fault of the VCFZ puts in contact intensely fractured Jurassic dolomites carbonates in the footwall block with Quaternary colluvial deposits in the hanging wall block. In the footwall block distinct structural units (CU1, CU2, and HSDZ; see Figures 3 and 4 for details) are recognizable based on different colors and damage intensity.

much less is known about the effects of structural inheritance on fault zone structure at the seismogenic source scale.

The Gran Sasso Ridge (GSR) is one of the main structural features of the Central Apennines (Figure 1) and consists of a stack of thrust sheets formed during Late Messinian to Middle Pliocene compression (Ghisetti & Vezzani, 1991). The uppermost portion of the antiformal stack is characterized by out-of-sequence thrusts exposed in the study area (i.e., the OMTZ; Ghisetti & Vezzani, 1991; Figure 1b). Early Pleistocene to Present extension is instead accommodated by active extensional fault zones, including the VCFZ described in this manuscript, cutting and partially inverting the inherited compressional structures (e.g., Demurtas et al., 2016). These faults affect a stratigraphic succession dominated by shelf and deep marine limestones and dolostones belonging to the Latium-Abruzzi platform (Parotto & Praturlon, 1975) including, from bottom to top, *Dolomia Principale* (Upper Triassic), *Calcare Massiccio* (Lower Jurassic), *Corniola* (Lower Jurassic), *Verde Ammonitico* (Lower-Middle Jurassic), *Calcari Bioclastici Inferiori* (Middle-Upper Jurassic), and *Maiolica Detritica* (Upper Jurassic-Lower Cretaceous) formations (Figure 1b; Adamoli et al., 2012; see Demurtas et al., 2016, for more details). The studied outcrops are mainly developed within the *Calcare Massiccio Fm.* which in the area consists of up to 600 m thick largely dolomitized, whitish to brownish limestone beds (5–50 cm thick) and intervals (1–5 m thick) organized in cyclothems (see Demurtas et al., 2016, for more details). The *Verde Ammonitico* Fm. consists of greenish to dark gray micrites with intercalations of marls and dark chert, which were overthrusted by the *Calcare Massiccio* Fm. (e.g., Adamoli et al., 2012; Ghisetti & Vezzani, 1991) and locally dolomitized (Figure 1b).

The VCFZ is an active extensional seismogenic fault belonging to the Campo Imperatore Fault System (CIFS), which runs for ~20 km in the Gran Sasso range and is thought to have generated at least three coseismic surface ruptures since Pleistocene times, with estimated magnitude up to $M_w = 6.95$ (Figure 1; Demurtas et al., 2016; Galadini et al., 2003; Galli et al., 2002). The VCFZ outcrops for ~5 km from the Vado di Corno pass to the base of Mt. Brancastello and borders to the north the upper part of the Campo Imperatore intermountain basin (Vezzani et al., 2010). In this study, we focused on an ~2 km long fault segment, which is spectacularly exposed between 1,600 and 1,950 m of altitude from the Vado di Corno pass eastward, within a series of subparallel incisions with badland morphology cutting through the fault zone footwall block (Figures 1 and 2). The incisions are up to 20–30 m deep, laterally continuous and provide the exposure to precisely map the three dimensional fault network at length scales of 1 to 100 m. The investigated fault network mainly cuts through dolomitic carbonates of the *Calcare Massiccio* Fm., estimated to be exhumed from a depth of 1–2 km (Agosta & Kirschner, 2003) with a cumulative extensional displacement of 1.5–2 km (Ghisetti & Vezzani, 1991). The hanging wall block of the VCFZ instead consists of glacial, alluvial, and colluvial deposits Late Pleistocene to Holocene in age (Adamoli et al., 2012; Giraudi & Frezzotti, 1995, 1997). The eastern limit of the studied fault segment was determined by the occurrence of a NE-SW trending inherited extensional fault zone separating a dolomitized region to the west from an undolomitized one to the east; in this way, within the selected area, the host rocks were homogenous in composition.

3. The VCFZ Structural Map

The high-resolution structural map of the VCFZ footwall block (Figure 3) was produced by mapping the outcrops of each incision at 1:500 scale (printed orthophotos 0.2 m/pixel were used as mapping base; courtesy of the Regione Abruzzo, www.geoportale.regione.abruzzo.it). The maps were then integrated in a GIS project including fault traces (categorized as master and subsidiary faults, and the latter according to their kinematics), fault and host rock outcrops (classified according to lithological composition and degree of fracturing), and other data (e.g., attitude measurements, samples, digital elevation model [DEM], and orthophotos). From the outcrop map (Figures S1 and S2 in the supporting information), an interpreted structural map was obtained by interpolation in the areas covered by scree deposits. The interpreted map and other relevant data were imported in MOVE (ww.mve.com), where six cross sections were reconstructed (Figure 4).

The structural map indicates that the VCFZ consists of an array of extensional fault surfaces with dominant WNW-ESE strike, mostly dipping to the SSW (Figure 3). The mapped portion of the fault zone affects, from top to bottom, a SW dipping monocline of dolomitized *Calcare Massiccio*, the OMTZ and some strongly deformed *Verde Ammonitico* beds (outcropping in tectonic windows and still part of the OMTZ; Demurtas et al., 2016). Five distinct structural units, showing a different degree of fracturing and/or cataclastic deformation, were mapped (see Demurtas et al., 2016): (i) Low Strain Damage Zone (LSDZ), (ii) High Strain Damage Zone (HSDZ), (iii) breccia unit (BU), (iv) Cataclastic Unit 2 (CU2), and (v) Cataclastic Unit 1 (CU1) (Figure 3). Individual fault strands were grouped according to their relative age, attitude, and kinematics. Fault surfaces genetically related to the VCFZ are classified as synthetic extensional (SSW dipping), antithetic extensional (NNE dipping), and transverse extensional (NNE-SSW striking). Fault surfaces originally related to the OMTZ, then involved in the VCFZ activity, are classified as inverted frontal ramps (synthetic faults associated with the BU), inverted lateral ramp (transverse extensional faults associated with the BU), and tear faults (NNE-SSW striking subvertical strike slip faults) (Figure 3).

3.1. Damage Zone Units (HSDZ and LSDZ)

The HSDZ and LSDZ (green and blue in Figures 3 and 4) represent the damage zone of the extensional VCFZ. They affect the whole outcropping sequence (*Calcare Massiccio* and *Verde Ammonitico*). The damage zones are affected by variable fracture intensity, mainly due to the occurrence of joints and minor calcite and dolomite veins. Subsidiary faults, both synthetic and antithetic, are also present. The low- and high-strain damage zones (Figure 3) were mapped based on fracture abundance, which was much lower for the low-strain unit (areal fracture intensity ~2 m^{-1} for a range of fractures length 0.4–1.1 m), compared to the high-strain one (areal fracture intensity ~120 m^{-1} for a range of fractures length 0.01–0.1 m). Moreover, primary sedimentary fabrics (e.g., bedding surfaces, stromatolitic laminations, and planar trails of fenestrae) are well preserved only in the LSDZ (see Demurtas et al., 2016, for details).

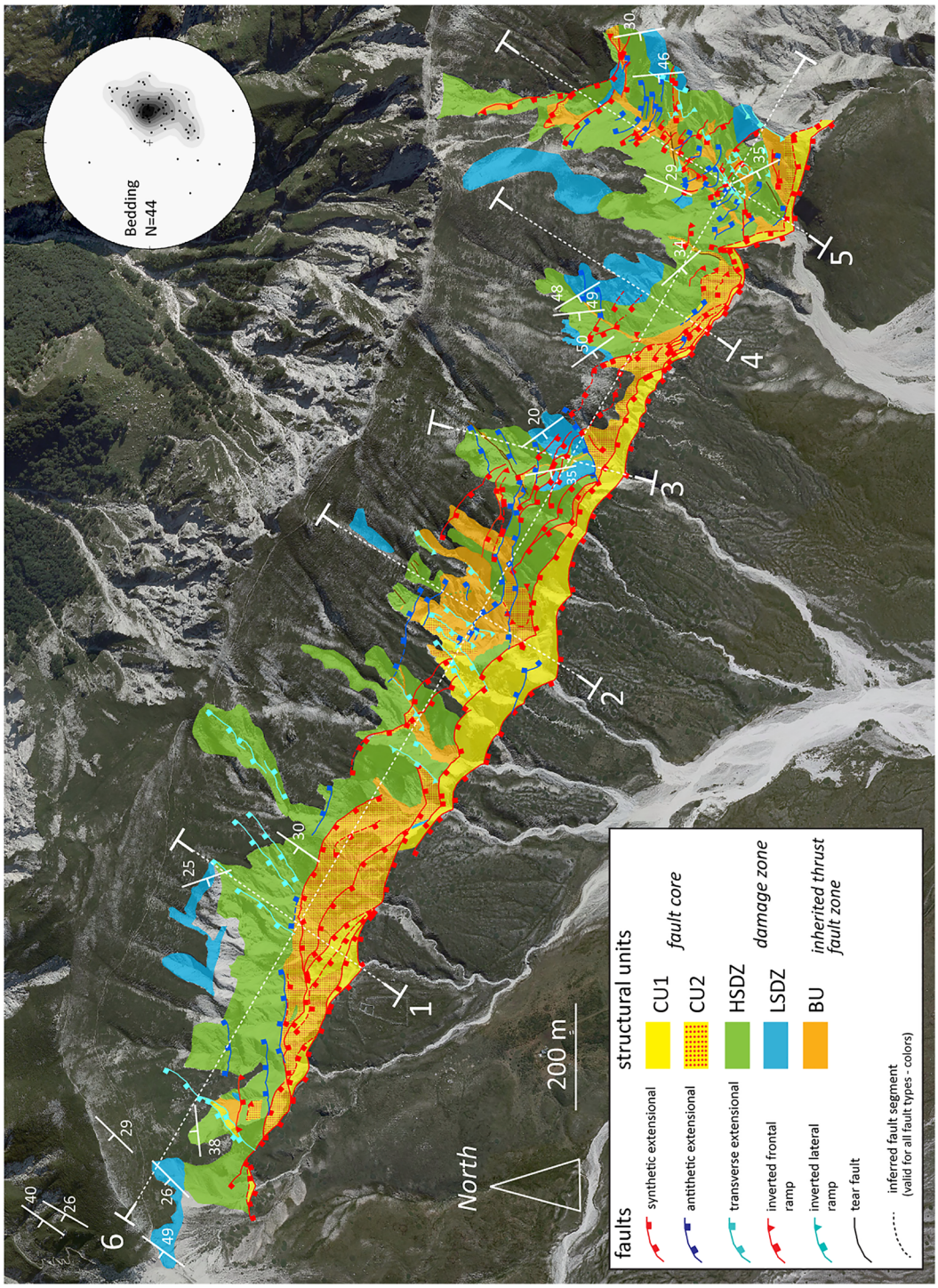

Figure 3. Structural map of the VCFZ footwall block. Distinct structural units are distinguished with different colors: fault core cataclastic units (CU1) and (CU2) in yellow and red dotted yellow, respectively; high-strain damage zone (HSDZ) in green; low-strain damage zone (LSDZ) in blue; and breccia unit (BU) in orange. The BU represents an older thrust fault zone (OMTZ) (Ghisetti & Vezzani, 1991). Master and subsidiary faults are bounding the structural units and have been distinguished as synthetic extensional, antithetic extensional, transverse extensional, inverted frontal ramps, inverted lateral ramps, tear faults, and inferred fault segments. The plot in upper right corner is a lower hemisphere stereographic projection with contours of the poles to cumulative bedding data measured in the area and displays the occurrence of a low-angle W-SW dipping monocline. Selected representative bedding data are in white symbols (the number refers to the dip angle). Traces of the six cross sections of Figure 4 are indicated with white dashed lines.

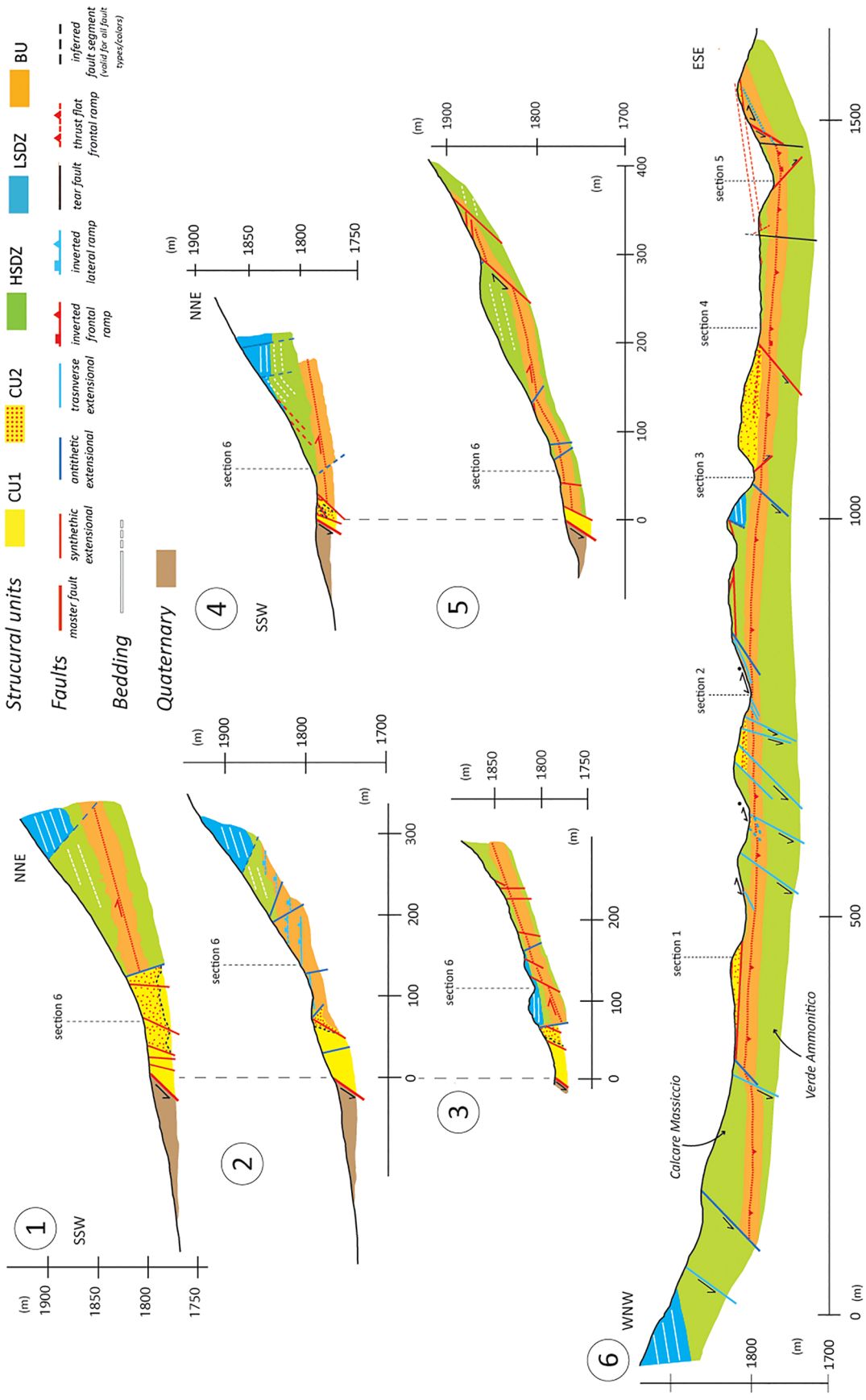

Figure 4. Cross sections of the structural map in Figure 3. Sections 1–5 are oriented perpendicular to strike moving from west to east and looking to the west, while Section 6 is parallel to fault strike looking to the north. The color code of both structural units and faults is indicated in the top right of the figure and is consistent with Figure 3. Bedding is displayed in white with a full (well recognizable in the outcrop) or dashed line (hardly recognizable in the outcrop). The bedding shows local dragging in proximity with the fault core units.

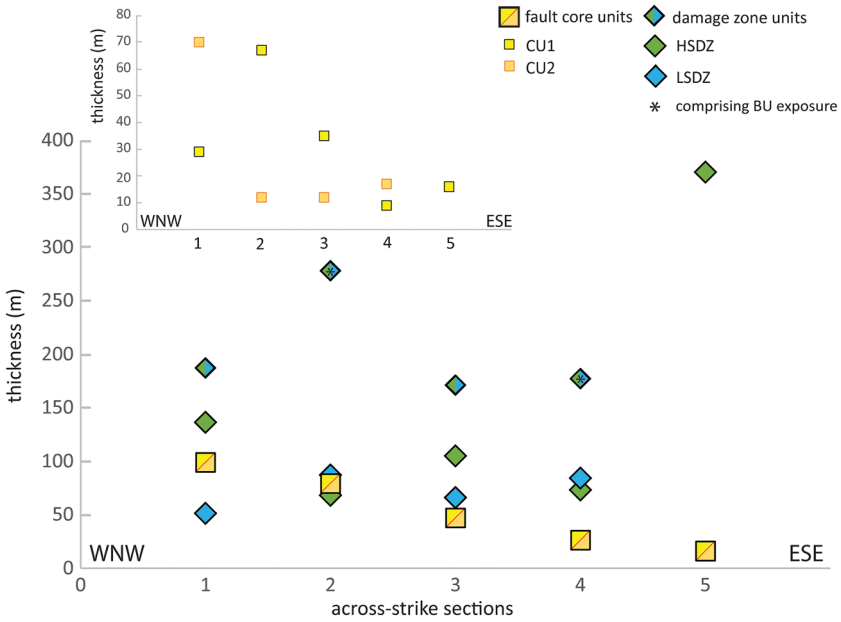

Figure 5. Thickness of VCFZ structural units derived the cross sections of Figure 4. Thickness data are reported both as individual and cumulative for the fault core and damage zone units. A general thinning of the fault core units occurs moving from west to east along VCFZ strike. For more details and data discussion see the main text.

The maximum exposed thickness of the damage zone (LSDZ + HSDZ) is in the 180–370 m range and broadly increases toward the east (Figures 4 and 5). In particular, the exposed HSDZ has a thickness range of 70–370 m, with the maximum values toward the eastern limit of the mapped fault zone segment. The portion of LSDZ exposed in the map is narrower, with a thickness range of 50–100 m, and mainly occurs in the upper part of the slope at larger distances from the Vado di Corno master fault (Figures 3 and 4). No host rocks affected by only background deformation have been identified within the mapped area; hence, we can only measure a minimum thickness of the damage zone. A few isolated lenses of LSDZ are locally embedded within the HSDZ at smaller distance from the fault core (Figure 3).

3.2. BU

The BU (orange in Figures 3 and 4) crops out as a pellicular layer at the bottom of some of the incisions, where it mimics the attitude of the gently SSW dipping OMTZ, which controls the ground morphology (Sections 1 and 3–5 in Figure 4). Additional exposures occur in the upper portion of the slopes, where inverted frontal and lateral ramps of the OMTZ outcrop (Figure 3; Sections 2, 5, and 6 in Figure 4). The BU separates the Middle Jurassic Verde Ammonitico formation in the footwall, from the dolomitized Lower Jurassic Calcare Massiccio in the hanging wall. Remnants of Verde Ammonitico are preserved as shear lenses within the BU or occur in more continuous exposures within small tectonic windows. The BU represents the exhumed OMTZ and consists of very peculiar fault rocks showing evidence of pervasive secondary dolomitization and dolomite veining (Demurtas et al., 2016). At the outcrop scale, the BU consists of greenish to nut-brown fault rocks, which can be classified as cohesive crush breccias (sensu Sibson, 1977) or mosaic to crackle breccias (sensu Mort & Woodcock, 2008) cemented by secondary dolomite (Figures 6a–6d and Demurtas et al., 2016, for more details). Based on the six cross sections (Section 6 in Figure 4), the thickness of the BU is estimated to be ≥20 m (this is a minimum thickness since the base of BU is not outcropping). The BU is overprinted by the extensional damage zone of the VCFZ, including both synthetic and antithetic WNW-ESE striking subsidiary fault surfaces, and is truncated by the fault core units (Figure 4, Cross Sections 1–5).

3.3. Fault Core Cataclastic Units (CU1 and CU2)

The cataclastic units make up the core of the VCFZ. CU1 and CU2 (respectively, yellow and red dotted yellow in Figure 3) were differentiated based on macroscopic criteria such as average grain size and color of

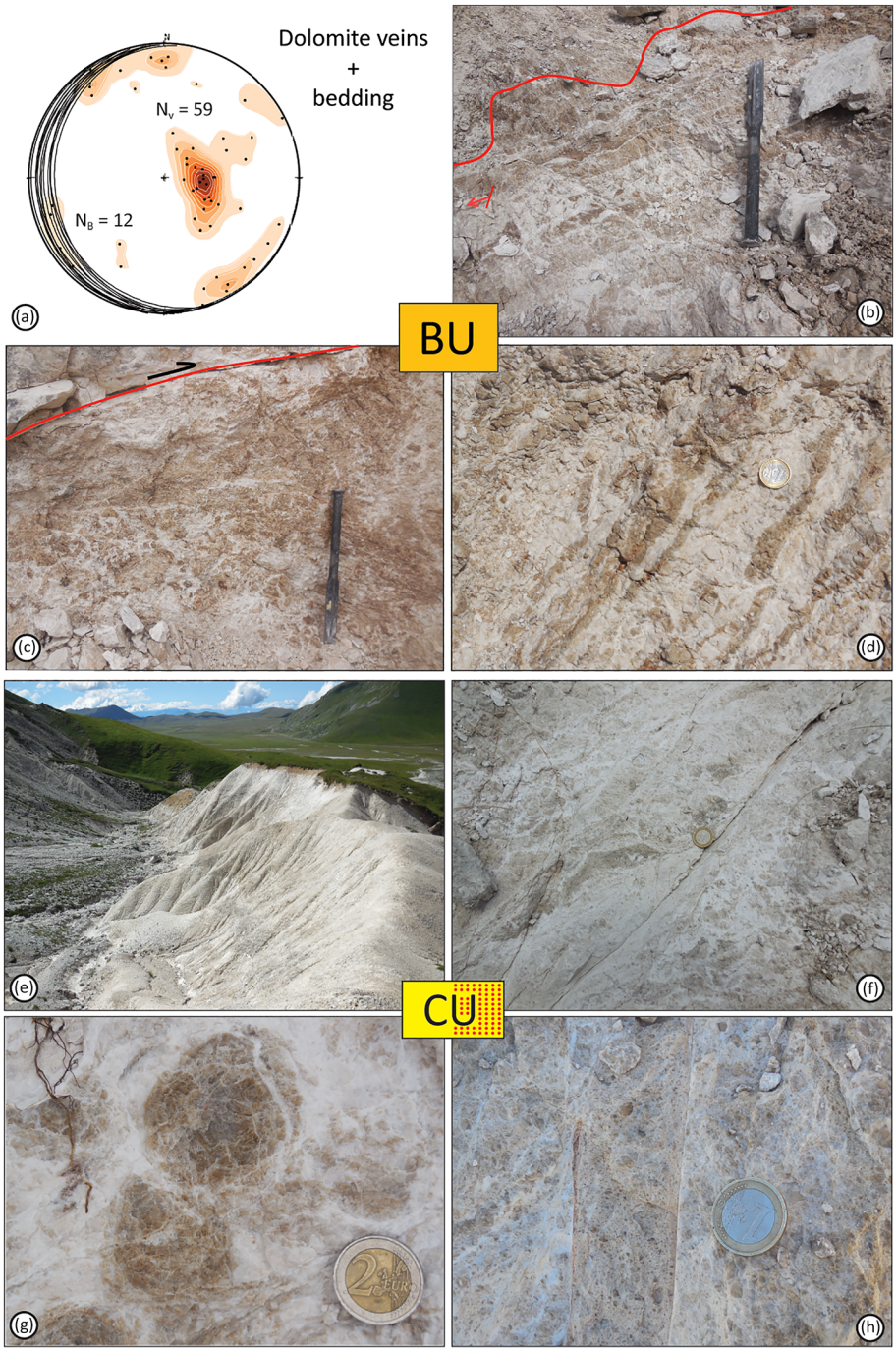

Figure 6. The breccia (BU) and the fault core cataclastic units (CU1 and CU2). (a) Equal area-lower hemisphere stereographic projection with contours of poles to dolomite veins within the BU. Black great circles refer to bedding planes where the BU lies in a flat geometry. Dolomite veins are peculiarly parallel to low-angle bedding surfaces (in flat thrust sections) or they are steeply dipping (dip angles of 70–85°) perpendicular to the thrust zone. (b) Breccia unit with wavy upper boundary toward the intensely fractured HSDZ. Note the up to 10 cm thick white dolomite bands associated to thrust-related secondary dolomitization. The local attitude of the thrust flat is indicated by the red arrow. (c) Outcrop exposure of the BU with a nicely developed breccia texture characterized by few centimeters in size nut in color dolostones clasts embedded within a whitish dolomitic cement. (d) Details of the banded texture within the BU related to thrust related secondary dolomitization. (e) Oblique down dip view of the VCFZ cataclastic core. The contact between the whitish highly fragmented carbonates and the reddish colluvial deposits represents the trace of the master fault which can be nicely followed along strike in the picture. The fault core is ~30 m thick and consists of cataclasites to ultracataclasites with various degree of textural maturity (CU1 vs. CU2) with finer grain sizes resulting in more white macroscopic colors (CU1). (f) Discrete fault sharply cutting through CU2. Grayish lenses of in situ shattered dolostones are recognizable within CU2. (g) Detail of an intensely fractured chert nodule preserved within the CU2. The rock is fractured down to the millimeter scale without significant shear deformation. (h) Multiple sharp mirror-like slip surfaces cutting through the ultracataclastic CU1.

nonweathered fault rocks (a proxy for the maturity of the fault rock fabrics). Both CU1 and CU2 consist of fault rocks pertaining to the "cataclastic series," from protocataclasites to ultracataclasites (Figures 6e–6h; Sibson, 1977). They are arranged in shear lenses bounded by synthetic extensional fault segments and elongated along the fault zone strike. All the mapped subsidiary faults within the damage zone are associated with cataclastic to ultracataclastic layers down to few centimeters thick, which are too thin to be represented in the structural map (Figure 3). The fault core thickness (CU1 + CU2) is highly variable in a range of 10–100 m and progressively narrows moving eastward along the fault zone strike (from Sections 1–5 in Figures 4 and 5; Figure 6e).

The CU2 consists of gray to brownish protocataclasites and cataclasites containing lenses, up few meters in size, of rocks that are fragmented down to the millimeter scale and do not show any distortion of the original protolith fabric (Demurtas et al., 2016; Figure 6g). For instance, preservation of dark brown shattered chert nodules derived from the *Verde Ammonitico* Fm. is common where the CU2 cuts through the BU (Figure 6g). The CU2 has an average thickness of 10–20 m in the central and eastern parts of the mapped fault zone segment and reaches values up to 70–100 m in the western portion of the fault zone (Section 1 in Figures 4 and 5).

The CU1 is a whitish ultracataclasite cemented by calcite, which locally contains lithons of CU2 up to tens of meters in size, bounded or crosscut by subsidiary faults with extremely localized slipping zones (<1–2 cm thick; Figures 6f and 6h). Such slipping zones display mirror-like slip surfaces sharply truncating dolostone and calcite clasts (grain size <10 mm), intensely sheared calcite-bearing veins with foam-like microtextures, localized mixed calcite-dolomite foliated cataclasites and fluidized ultracataclasites (see Demurtas et al., 2016, for details about slip zones microstructures). The CU1 has a highly variable thickness along the VCFZ strike, in the range 10–70 m, controlled by the master fault segmentation. The minimum thickness (~10 m) occurs at the eastern limit of the mapped master fault, while the maximum one (~70 m) is in the central western sector (Section 2 in Figure 4) and derives from the superposition of two right-stepping master fault segments (Figures 3 and 4).

4. Orientation and Kinematic Data

Structural and kinematic data (1,815 data consisting of faults/joints/veins attitude and fault slip vectors) were measured at localities evenly distributed across the outcrops and located using handheld GPS (accuracy typically ±2 m). In particular, 282 fault slip data were collected along the entire fault zone. The sense of slip was defined based on across-fault separations and brittle kinematic indicators (e.g., Riedel shears, S-C fabrics, grooves, and/or calcite fibers on slickensides; Chester & Logan, 1987; Petit, 1987; Petit et al., 1983).

In this section, we briefly describe the orientation and kinematic data collected within the damage zone and fault core of the VCFZ (Figure 7). As a general feature, synthetic extensional faults are evenly distributed within the VCFZ, while high-angle (dip angle >70°) antithetic and transverse faults are more abundant within the damage zone (HSDZ, LSDZ and BU; see map distributions in Figures 3 and 7).

4.1. Damage Zone

Only few subsidiary faults were recognized in the HSDZ and LSDZ units, whereas faults are abundant in the BU, where they are arranged mainly in two sets: a low-angle (dip angles 20–40°) WNW-ESE striking one and a high-angle (dip angles 40–75°) N-S to NE-SW striking one. Many of these Quaternary extensional faults have dip-slip to oblique-slip kinematics (pitch angles 30–90°) and exploit preexisting SSW dipping thrust frontal ramps and NW dipping lateral ramps (Figures 7 and 8). Extensional reactivation of thrust flat segments is minimal and seems to occur at very local scale (i.e., thrust flats are typically crosscut by normal faults rather than being reactivated in extension).

Joints in the damage zone are steeply dipping (dip angles 60–90°) and strike from WNW-ESE to E-W moving westward along the fault zone. Joint orientation is consistent with that of the Quaternary extensional faults cutting the fault core rocks and is not influenced by the protolith (i.e., dolomitized *Calcare Massiccio* in the HSDZ and LSDZ or the BU).

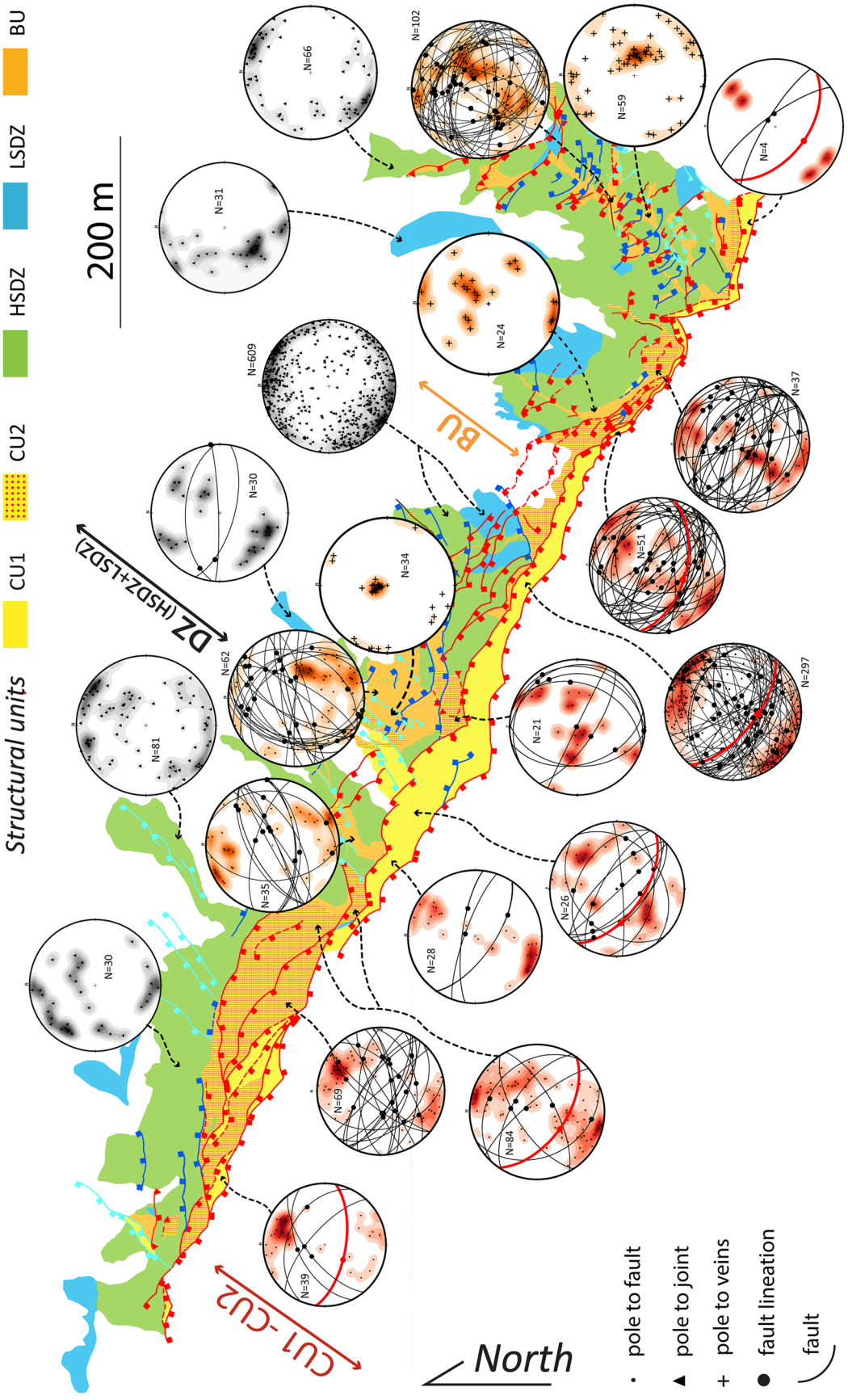

Figure 7. Structural data of the VCFZ. Equal area-lower hemisphere projection of structural data collected within the different structural units (the rough position of data collection is indicated with dashed arrows). CU1-CU2: small black dots with red contours are poles to faults, black great circles with big black dots are faults with slip directions, and red great circles with big red dots are master fault with slip directions. BU: small black dots with orange contours are poles to faults, black great circles with big black dots are faults with slip directions, and small black crosses with orange contours are poles to dolomite veins. HSDZ+LSDZ (plots are all cumulative within the damage zone): black triangles with black contours are poles to joints, and black great circles are faults with measured slip directions (big black dots). Reported fault slip data are extensional (the upper block is moving down), and are the one used for the kinematic analysis (Section 6, Figure 9).

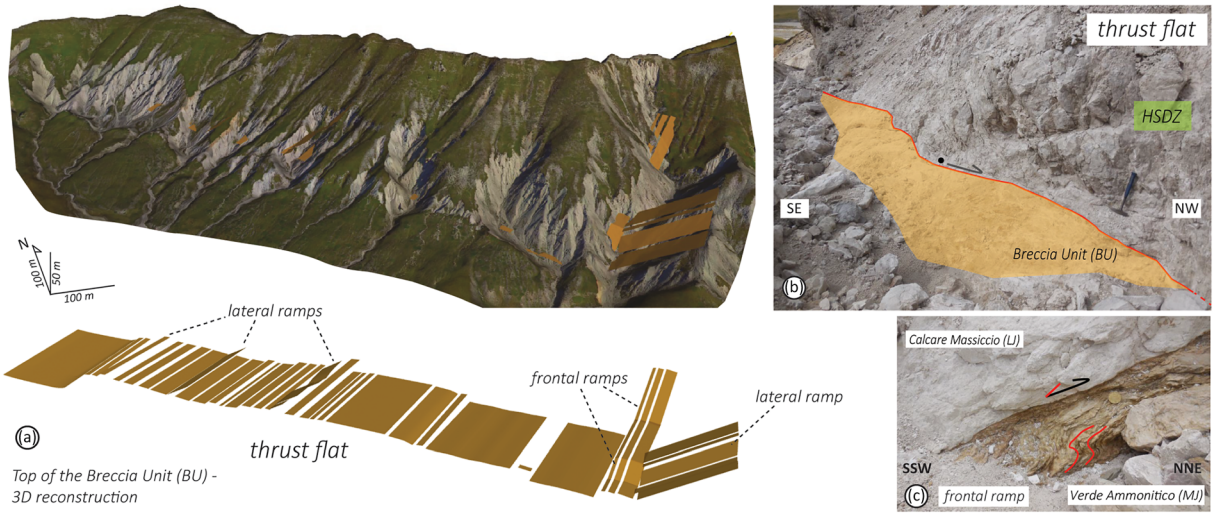

Figure 8. Geometry of the breccia unit (BU)-OMTZ. (a) Three-dimensional reconstruction of the top (i.e., contact with the HSDZ and LSDZ) of the BU and relations with the topography. The upper image shows the culminations and intersections of the BU top with topography (i.e., a DEM draped with an ortophotomosaic of the study area). The lower image depicts the geometry of the BU top (the same of the upper image) without the topography. The thrust zone consists of a SSW gently dipping flat with a noncylindrical geometry characterized by three small lateral ramps in the western fault zone sector and a big one at the eastern termination of the mapped fault zone segment. The latter fault zone sector is also characterized by two big frontal ramps segmenting the thrust flat across strike. The occurrence of extensional faults in correspondence to frontal and lateral ramps is not displayed in this reconstruction. (b and c) Outcrop exposures of the BU in a flat-like (b) and a frontal ramp (c) setting with thrust-like stratigraphy (Lower Jurassic *Calcare Massiccio* on top of Middle Jurassic *Verde Ammonitico*). In the case of the frontal ramp, extensional dragging of the foliation (curved red lines in the figure) in the footwall cataclasites suggests a negative inversion of the ramp (see also Demurtas et al., 2016).

4.2. Fault Core Cataclastic Units (CU1 and CU2)

Subsidiary faults accommodating Quaternary extension are abundant in the fault core and are arranged in two WNW-ESE striking sets: a SSW dipping synthetic dominant set and a NNE dipping antithetic set. Fault kinematics is mainly dip slip, with a small oblique component (pitch angle between 65° and 90°; Figure 7). The average WNW-ESE fault strike rotates to E-W in the western sector of the mapped VCFZ segment. Moreover, two NW-SE striking fault sets (synthetic and antithetic) and minor N-S to NNE-SSW striking faults occur in the central sector of the fault zone, where CU1 is thicker and master slip surfaces are segmented with en echelon geometry (Figure 7).

5. Structural Inheritance

The structural control of the OMTZ on the subsequent extensional fault pattern is indicated by extensional S-C fabrics and drag folds overprinting the low-angle faults with thrust-like stratigraphic separation (mainly frontal ramps; Figure 8c). Based on the structural data collected throughout the mapped VCFZ segment, we were able to reconstruct the geometry of the top of BU in three dimensions, representing with a good approximation the geometry of the OMTZ in this area (Figure 8a). The BU consists of an ~2 km long, WNW-ESE striking and gently SSW dipping layer (dip angle ~15°), characterized by a noncylindrical geometry. Indeed, moving from west to east the BU top displays lateral undulations culminating in three small lateral ramps in the western fault zone sector and a big one at the eastern termination of the mapped area. The eastern sector of the BU is characterized by a more complex geometry due to the occurrence of two big frontal ramps segmenting the thrust flat across strike.

6. Kinematic Analysis

Kinematic data were analyzed with FaultKin software, following Marrett and Allmendinger (1990), to reconstruct the orientation of kinematic (*P* and *T*) axes. Average *P* and *T* axes, calculated using linked Bingham statistics, were used to summarize fault kinematics and to provide a first-order approximation of

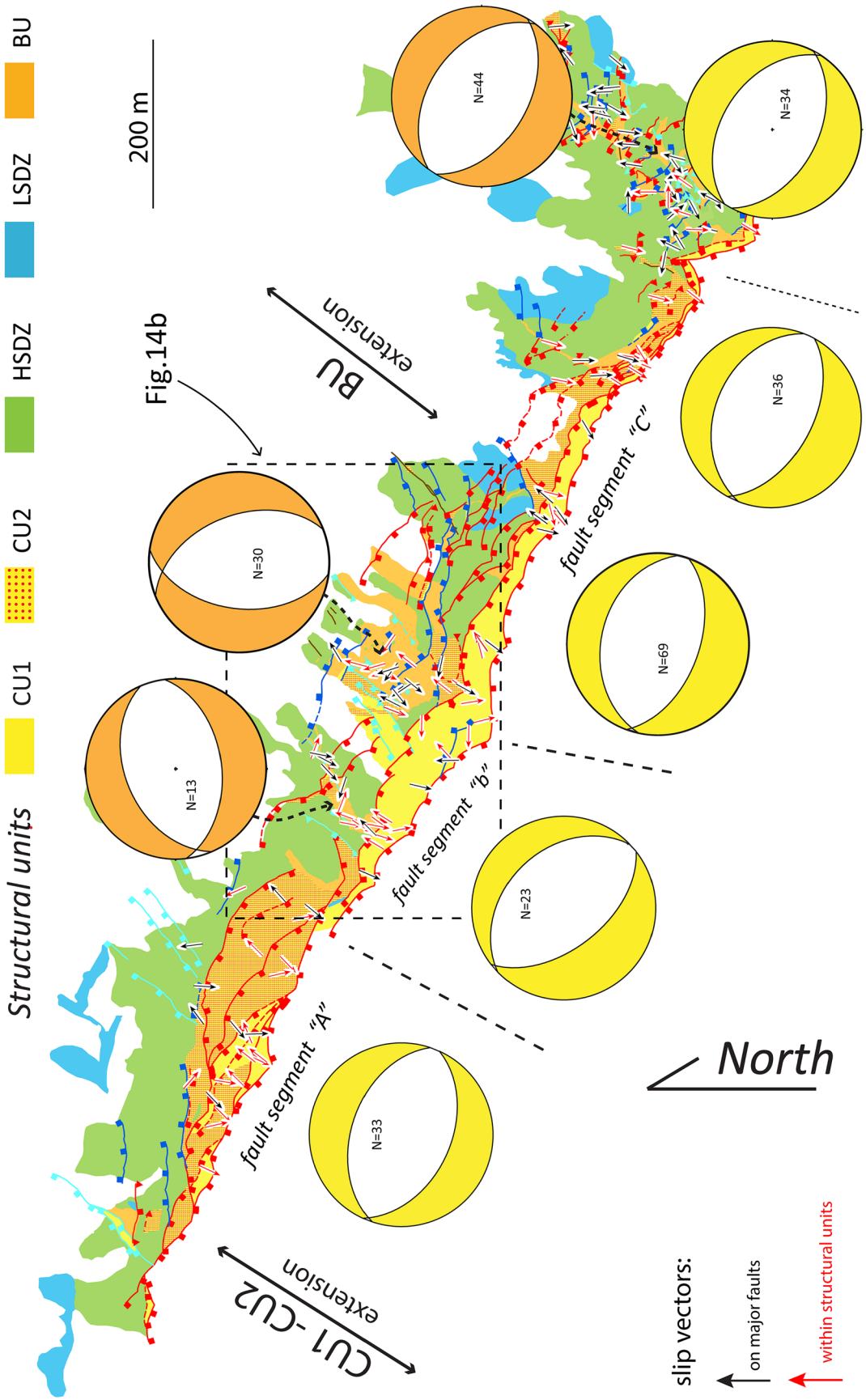

Figure 9. Kinematic analysis of the VCFZ. Kinematic analysis of fault slip data was performed on five different structural blocks within the VCFZ (divided by dashed lines), moving along the fault strike. Calculated kinematic *P* and *T* axes were graphically represented by beach balls stereoplots, one for each structural block. Yellow beach ball stereoplots display the results of kinematic data inversion in extension for fault core cataclastic units (CU1 and CU2). Orange beach ball stereoplots display the results of kinematic data inversion in extension for breccia unit (BU). The distribution of the slip vectors measured on faults with precise location is represented in the map; black arrows are slip direction measured on major faults reported in the map, while red arrows are slip direction data collected on subsidiary faults (too small to be reported in the map) within the structural units. Beach balls with fault slip data are shown in Figures S3 and S4 of the supporting information. See the main text for a detailed description of the kinematic map. Dashed rectangular inset refers to the detail of Figure 14b.

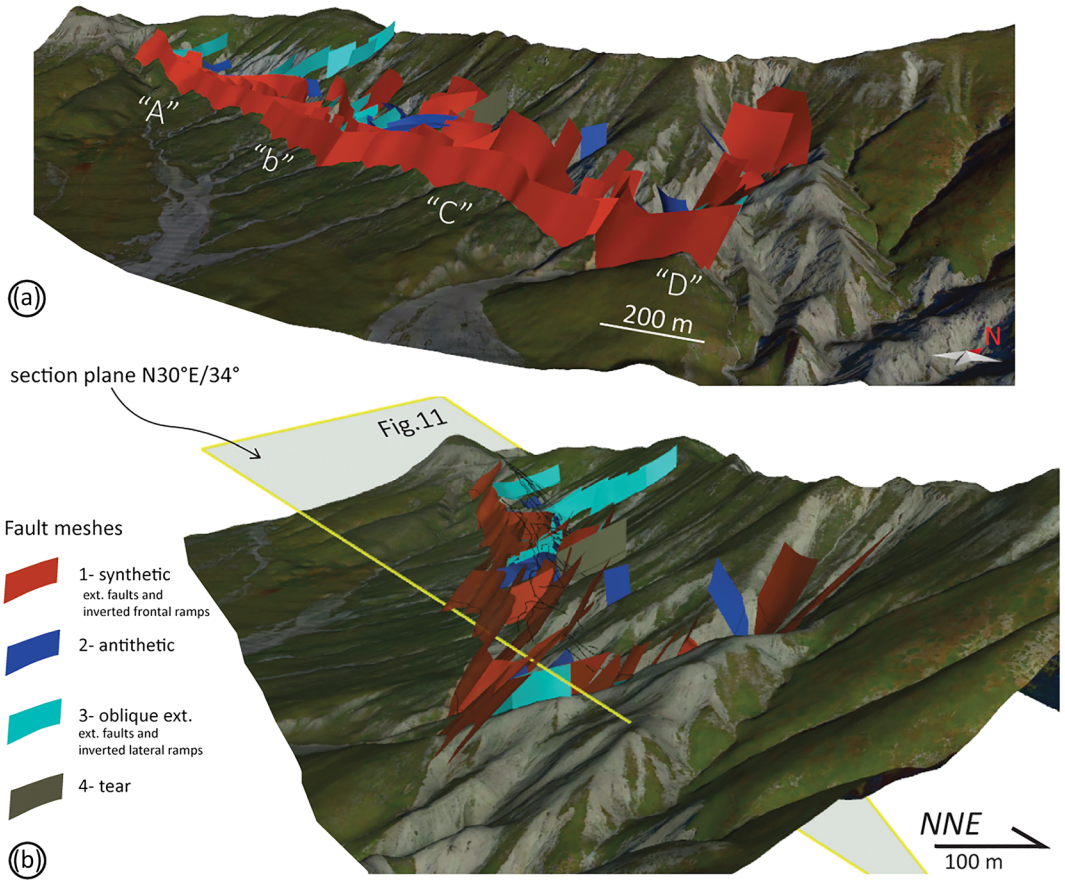

Figure 10. Three-dimensional fault mesh model of the VCFZ. Along-strike (a) and across-strike (b) view of the fault mesh structural model. Both views highlight the segmentation of the master fault surface, which is arranged in two main WNW-ESE striking right-stepped segments (Segments "A" and "C") linked by a shorter, NW-SE striking one (Segment "b"), located in the central sector of the mapped area and associated with shorter E-W striking linkage faults. Synthetic fault surfaces are in red and comprise extensional faults and inverted frontal ramps of the OMTZ. Antithetic fault surfaces are in blue. Oblique extensional fault surfaces are in light blue and comprise extensional faults and inverted lateral ramps. Tear fault surfaces are in gray. The section plane in the across-strike view contains the 2-D fault network analyzed in Figure 11.

incremental strain tensors within the VCFZ, pending the assumptions of kinematic compatibility and scale invariance (sensu Marrett & Allmendinger, 1990).

The kinematic analysis of the VCFZ was performed to investigate the occurrence and spatial distribution of kinematic complexities within the more intensely deformed structural units and their relations with the geometry of both compressional inherited and extensional fault networks. Kinematic analysis of fault slip data was performed on five different structural blocks (~300 m wide) within the VCFZ, moving from east to west along the fault strike (Figure 9). The blocks roughly correspond to the areas cut by the cross sections of Figures 3 and 4. In all structural blocks, kinematic data from the fault core (CU1 and CU2) and the breccia (BU) units were inverted for an extensional tectonic framework. In the case of the BU, the kinematic inversion on fault surfaces originally related to the OMTZ (i.e., reactivation in extension of frontal/lateral thrust ramps) allowed us to estimate the effect of structural inheritance on later extension.

The calculated kinematic *P* and *T* axes were graphically represented by beach balls stereoplots, one for each structural block. The distribution of the slip vectors measured within the entire fault zone, both on mapped faults and smaller scale ones, was also represented in the kinematic map (Figures 9, S3, and S4). This helped to visualize the extension directions within the different structural units of the VCFZ, including slip partitioning between main fault surfaces and subsidiary ones, moving both across and along the fault strike.

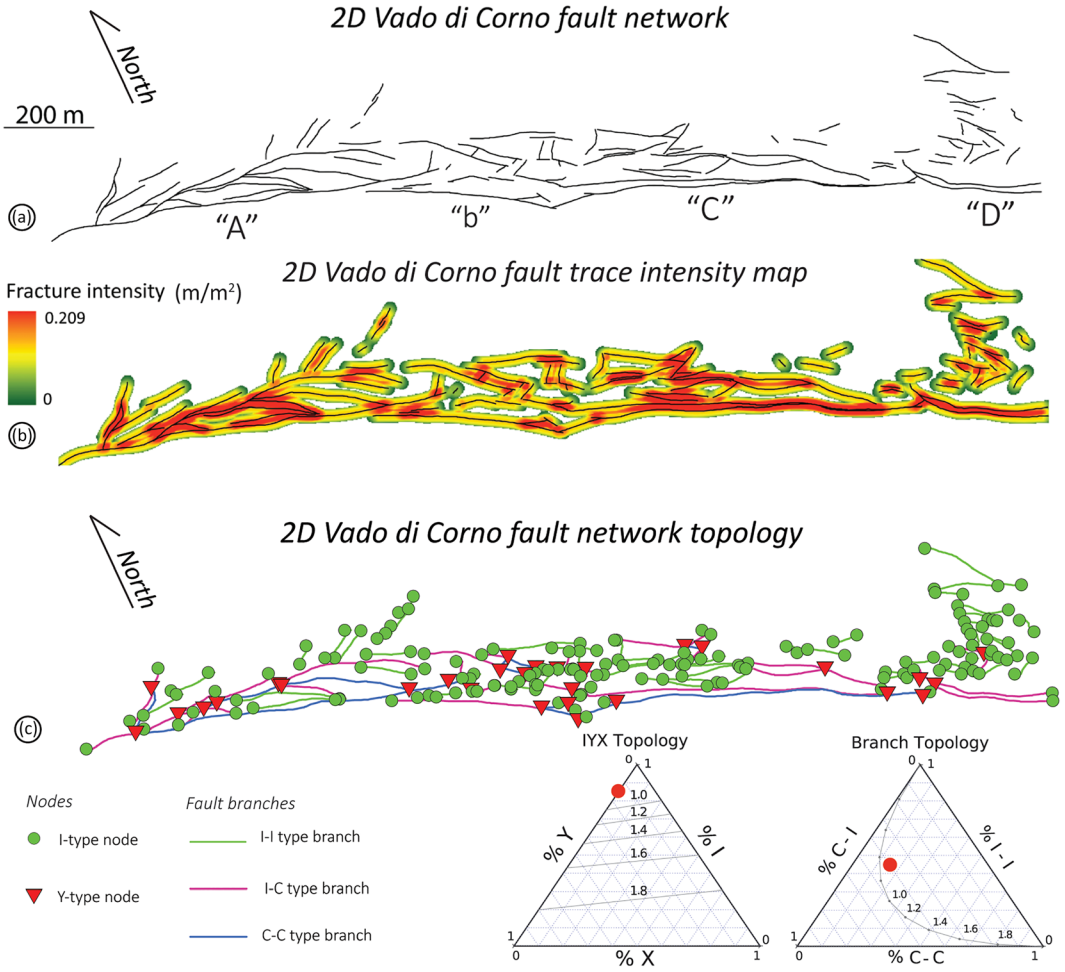

Figure 11. Two-dimensional VCFZ network geometry and topology. (a) Two-dimensional VCFZ network derived from the sectioning the 3-D VCFZ model (Figure 10b). The different segments of the VCFZ master fault, already distinguished in Figure 10, are clearly recognizable. (b) Two-dimensional fault trace intensity map of the VCFZ. The intensity is high both along the master and subsidiary faults in the eastern and western sector of the fault zone, while it is lower in the central portion of the fault zone. See the main text for more details. (c) Topological map of the VCFZ, showing the distribution of nodes (I, Y, and X nodes) and branches (I-I, I-C, and C-C branches). Clustering of Y-type nodes (representing fault splays and abutments) in three clouds located in the east and west side of the mapped VCFZ, and in the central overstepping region, respectively, provides a proxy for the along-strike segmentation of the fault zone. Statistics of VCFZ nodes and branches topology are summarized in the ternary diagrams. See the main text for more details.

Beach ball plots and slip vectors from the fault core cataclastic units indicate an average NNE-SSW extension direction, accommodated mainly by WNW-ESE striking and SSW dipping faults (Figures 7 and 9). The kinematic analysis of the fault core pointed out the presence of at least two major fault segments, an eastern and a western one (Segments "A" and "C" in Figure 9), which are linked at an overstep region (Segment "b" in the central region of the map in Figure 9). The region of kinematic linkage is affected by NE-SW oriented extension, mainly accommodated by WNW-ESE to NNE-SSW striking and SSW to WNW dipping faults with an oblique (both left and right lateral) component (Figures 7 and 9).

Beach ball plots of the BU suggest a NNE-SSW oriented extension in the eastern sector accommodated by WNW-ESE striking faults with local reactivation of previous coaxial compressional structures (Figure 9). On the other hand, in the central and western sectors, extension is at higher angle to the average strike of the VCFZ and is accommodated by a dominant N-S to NE-SW striking fault set and minor subvertical ENE-WSW striking faults, both with oblique kinematics (Figures 7 and 9). The N-S to NE-SW structures

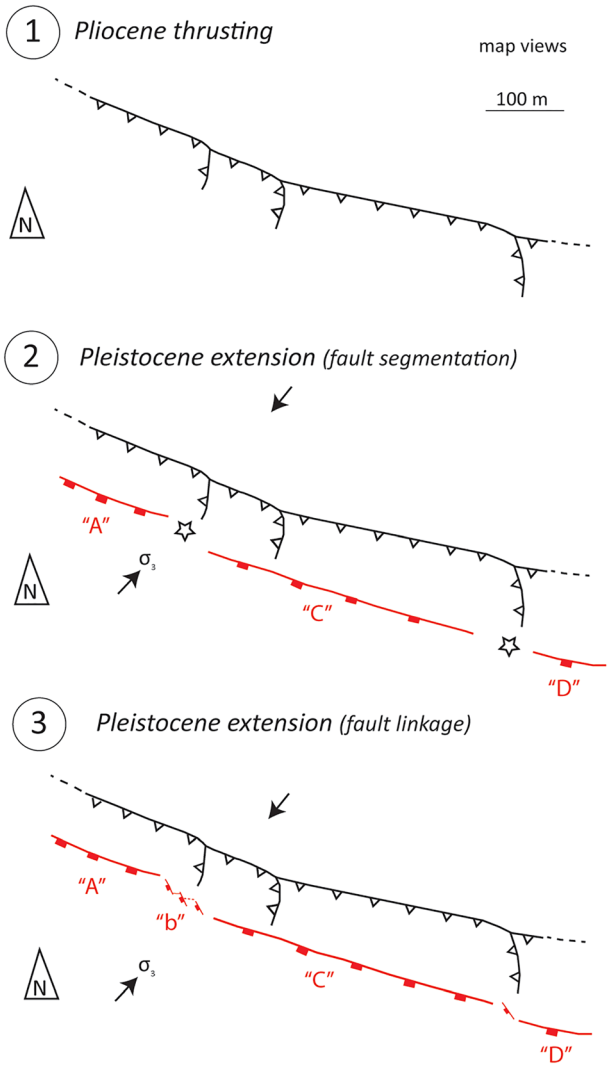

Figure 12. Three-stage conceptual model to explain the along-strike segmentation of the VCFZ master fault. See the main text for details.

mainly represent inherited lateral ramps of the OMTZ. Interestingly, the occurrence of this structural complexity within the BU corresponds to the location where the fault core is segmented and overstepped (Figure 9). Further evidence of this structural control is represented by the oblique (in strike and kinematics) subsidiary faults affecting the outer portion of the VCFZ core specifically at this location (i.e., CU2; see data in Figures 7 and 9).

7. Three-Dimensional Fault Network Model

A 3-D fault network model of the VCFZ was reconstructed using MOVE and SKUA-GOCAD (www.pdgm.com) starting from the interpreted structural map in Figure 3 (see supporting information for details about the modeling workflow; Caumon et al., 2007). This enabled us to obtain a realistic representation of the fault zone geometry in three dimensions, which represented one of the goals of this study and the base for subsequent analyses (sections 8–10).

Two views of the 3-D fault network model, one along and one across fault strike, are displayed in Figure 10. Both views highlight the segmentation of the master fault surface, which is arranged in two main WNW-ESE striking right-stepped segments (Segments "A" and "C," each ≥800 m long) linked by a shorter, NW-SE striking one (Segment "b" ~250 m long), located in the central sector of the mapped area and associated with few smaller (≤100 m long) E-W striking linkage faults (see Figures 7, 9, 10, and 11a). Similar NW-SE and E-W striking features occur in the easternmost side of the master fault surface and could represent a linkage structure with another longer fault segment to the east (Segment "D" in Figure 10). At scales <100 m, the two main fault segments ("A" and "C") of the master fault surface show strike variations from WNW-ESE to NW-SE. Large-scale synthetic subsidiary faults (red in Figure 10) are present in the eastern sector of the mapped VCFZ, up to distances >300 m from the master fault surface, while oblique fault surfaces (light blue in Figure 10) dominate the central and western portion of the VCFZ (see also Figures 3 and 9).

8. Two-Dimensional VCFZ Network: Geometry and Topology

Starting from the 3-D fault network model of the VCFZ, we quantified its geometry (i.e., spatial distribution and length of fault traces) and topology (i.e., type and distributions of nodes and branches) in two dimensions. To avoid geometrical distortion, we used an oblique cross section perpendicular to the average attitude of the VCFZ master faults (N210/56°). We calculated the intensity of macroscopic fault traces (total length of faults/sampling area, equivalent to P21; Dershowitz & Herda, 1992) in GIS, using circular scan areas with radius of 10 m, centered on cells of a regular grid with step size of 1.5 m. The two-dimensional topology of the fault network was characterized using the NetworkGT toolbox (Nyberg et al., 2018). Following Ortega and Marrett (2000), we calculated the following topological quantities of the VCFZ network: number of I (isolated), Y (abutting) and X nodes (crossing) and number of I-I (isolated), I-C (partially connected), and C-C (doubly connected) branches; results are conveniently represented in ternary diagrams (Barton & Hsieh, 1989). We also calculated the ratio given by number of branches over number of connections, which represents a proxy for the connectivity of the fault network (Manzocchi, 2002). We used both fault intensity and topology maps to depict the complexity of the VCFZ network and relate it to fault segmentation and structural inheritance.

The intensity map of macroscopic fault traces derived from the 3-D model shows values in the range 0–0.23 m/m^2. Because of the dependence from the dimension of the scan area, fault intensity values are

considered only in a relative sense, to analyze their spatial variations within the VCFZ. Fault intensity values are higher near fault intersections. In particular, intensities are high both along the master and subsidiary faults in the eastern and western sector of the fault zone (Segments "A," "C," and "D"), while they decrease in the central portion of the fault zone (Segment "b"; Figure 11b). Indeed, in the central portion of the VCFZ, the dominant WNW-ESE structural trend (both faults and shear lenses) is altered by the occurrence of oblique structures related to the noncylindrical geometry of the inherited thrust zone (see Figures 3, 8, and 11b).

In terms of topology (Figure 11c), the VCFZ network is characterized by a high number of I-type nodes (~85%), a lower number of Y-type nodes (~15%), and no X-type ones. Looking at the branch statistics, the VCFZ network consists of ~45% of C-C doubly connected branches, ~40% of I-I isolated branches, and ~15% of I-C partially connected branches. The calculated value of connections per branch (CB) for the entire VCFZ network is ~0.7 and indicates a relatively low level of connectivity of the fault network (see ternary diagrams in Figures 11c). Clustering of Y-type nodes (representing fault splays and abutments) in three clouds located in the east and west side of the mapped VCFZ and in the central overstepping region, respectively, provides a proxy for the along-strike segmentation of the fault zone. In particular, the relative abundance of Y-type nodes indicates a high complexity of the fault network, which further increases at linkage zones within the fault core and damage zone, where inherited structural complexities occur (i.e., lateral and frontal ramps of the older thrust zone). The spatial distribution of Y-type nodes is also strictly related to the distribution of partially and doubly connected fault branches (I-C and C-C) determining the structural style of the VCFZ, which is characterized by fault lenses elongated WNW-ESE, along the average strike of the fault zone.

9. Discussion

9.1. Structural Inheritance and Along-Strike Segmentation of the VCFZ

We have showed that across- and along-strike geometrical and kinematic irregularities in the extensional VCFZ fault zone are spatially associated with the structural complexity of the OMTZ thrust fault, including both frontal and lateral ramps (Figure 8). Kinematic analysis indicates that extension within the VCFZ has been occurring in a NNE-SSW direction and has been mainly controlled by the orientation of the preexisting thrust fault zone (Figure 9). This inference is supported also at a larger scale (e.g., Figures 1 and 2), by the evidence that the VCFZ and the CIFS mimic the strike of the Gran Sasso thrust system (GSR in Figure 1a). Since the latter consists of a stack of thrust sheets over few kilometers in depth, its structural control on the subsequent extensional faulting is thought to occur at crustal scale (see Figure S5; Ghisetti & Vezzani, 1990; Ghisetti & Vezzani, 1991; Lucca et al., 2019).

The along-strike segmentation of the VCFZ master fault surface, which is arranged in three fault segments with WNW-ESE average strike (see Figures 3 and 9–11), is constrained by field mapping, kinematic analysis, the three-dimensional structural model, and the topological analysis of the fault network. The main segments are the western and the central one ("A" and "C," each with exposed length of ~800 m), which bound almost entirely the mapped footwall area and are interacting at a right overstep region (Segment "b"; see Figures 3 and 9–11). The latter is dominated by NW-SE striking linkage faults and is the site where the maximum thickness (up to 70 m) of the fault core cataclastic unit CU1 occurs (Figures 4, 5, 7, and 9). The lateral termination of another WNW-ESE striking master fault segment ("D") likely occurs in the eastern limit of the mapped area (e.g., Figures 3, 9, and 11), where the Fault Segment "D" is linked with the central one by a NW-SE oriented fault (Figure 11).

To explain the along-strike segmentation of the master fault of the VCFZ, we developed a conceptual model that involves the development of a Pliocene E-W to WNW-ESE striking, nonplanar thrust fault zone, gently dipping to the S-SSW (Figures 8, 9, and 12; Ghisetti & Vezzani, 1991). From Pleistocene times onward, regional extension affected the area with an average NE-SW oriented maximum extension direction (assumed to be parallel to the minimum principal, subhorizontal, stress $\sigma 3$; e.g., Ferrarini et al., 2015; Lavecchia et al., 1994). Because of the inherited structural framework, the extensional VCFZ developed with the same strike of the older thrust zone (i.e., BU; Figures 8 and 9). Due to the noncylindrical geometry of the thrust fault zone, the VCFZ master fault was segmented in three WNW-ESE striking segments ("A," "C," and "D") (Figures 9–11). The segmentation localities (indicated by stars in Figure 12) coincide with the structural positions of the thrust lateral ramps. At segmentation localities and in the overstepping regions, inherited

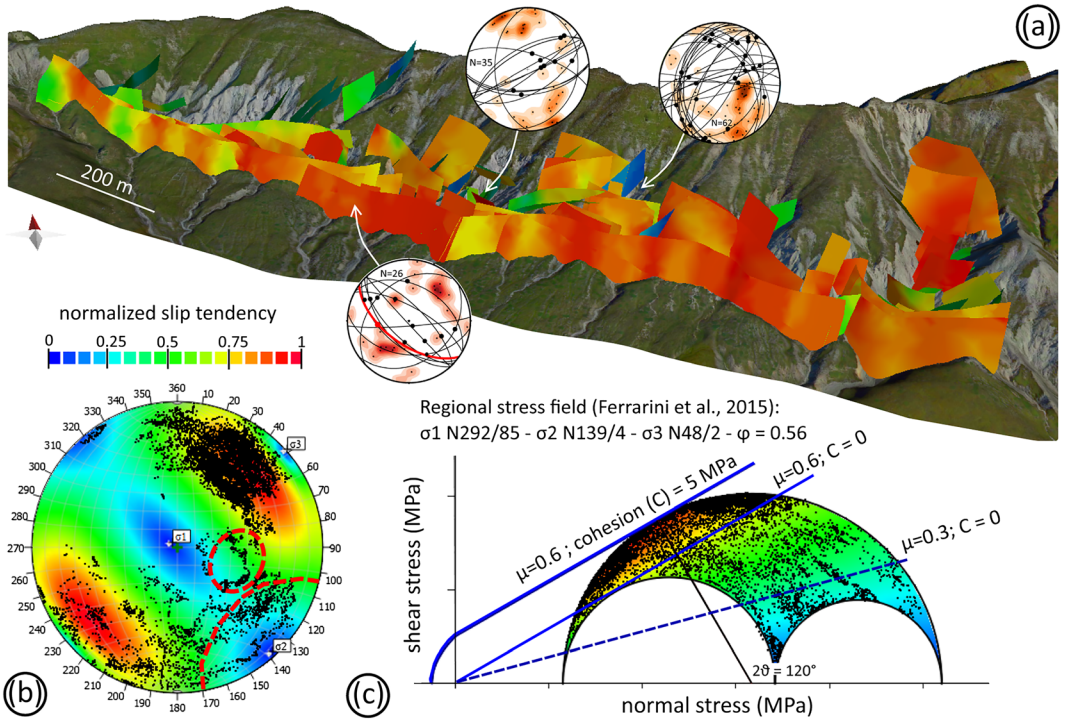

Figure 13. (a) Three-dimensional slip tendency analysis of the VCFZ. The normalized slip tendency (NTs) was calculated for each triangular face on the three-dimensional fault meshes (i.e., bigger faults contribute with more data in the plots b and c). The orientation of the three-dimensional stress tensor and the shape ratio was derived from Ferrarini et al. (2015). Stereoplots representing well-oriented NW-SE striking faults within CU1 and transverse structures within the BU are added to the model (the stereoplots are taken from Figure 7). (b) Stereoplot with orientation and NTs values of the fault surfaces of the 3-D VCFZ model. Red dashed circles indicate the orientation of transverse structures (lateral ramps and tear faults) with NTs < 0.4. (c) Orientation and NTs values of the fault surfaces in the Mohr space. Blue lines represent three failure/sliding envelopes respectively for (i) "strong" newly formed faults ($\mu = 0.6$, cohesion = 5 MPa), (ii) "strong" preexisting faults ($\mu = 0.6$, no cohesion), and (iii) "weak" preexisting faults ($\mu = 0.3$, no cohesion).

lateral ramps were reactivated with oblique kinematics and eventually new NW-SE striking linkage faults, well oriented with the current regional extension direction, developed (Figure 12).

The thickness of the fault zone is also related to its along-strike segmentation (Figures 3 and 4). This is particularly evident for the HSDZ, which display a thickness increase at segmentation localities (Figures 4 and 5), thus suggesting a growing mechanism of lateral fault linkage (Delogkos et al., 2020; Mayolle et al., 2019). The fault core thickness (CU1 + CU2) decreases moving from west to east along fault strike, but the more intensely deformed cataclastic unit (CU1) reaches its maximum thickness at the overstep between Segments "A" and "C." This location might correspond to an area of higher displacement accommodation at the scale of the entire VCFZ, assuming that the different segments of the master fault merge into a single larger one at depth.

The case of the VCFZ is a relevant example of how structural inheritance strongly influences the structure of extensional fault zones at different scales (from kilometers to tens of meters). Similarly, several recent studies demonstrated how the geometry and kinematics of extensional faults during rifting, especially in the early stages, are intimately controlled by the occurrence of preexisting fabrics and structural weaknesses within the basement (e.g., Collanega et al., 2019; Hollinsworth et al., 2019; Kirkpatrick et al., 2013; Kolawole et al., 2018; Philips et al., 2016; Williams et al., 2019). In particular, our detailed investigation at the scale of the internal structure of a single fault zone can give relevant insights to interpret structural inheritance relationships imaged at regional scale in 3-D seismic data (e.g., Phillips et al., 2019).

9.2. Geometrical and Kinematic Complexities During Extension

Here below, we discuss some implications of the proposed conceptual model for the development and segmentation of the VCFZ (Figure 12) with a slip tendency analysis and a mechanical (BEM elastic) model in

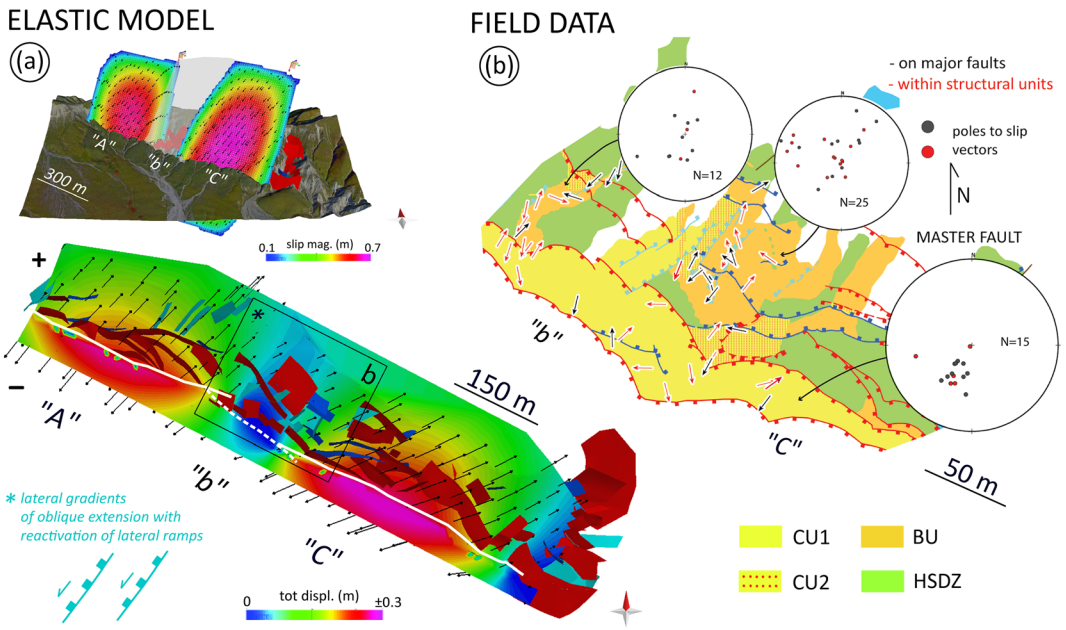

Figure 14. (a) Three-dimensional BEM elastic model of the VCFZ. Upper portion: extended master fault surfaces "A" and "C" with calculated slip distributions. Maximum slip magnitude is ~0.7 m with a small oblique component. Fault Segment "b" is represented as a transparent gray surface since it is not considered in the modeling. Lower portion: distribution of total displacement on the observation surface (positive with relative uplift in the footwall block and negative with relative lowering in the hanging wall) produced by slip accumulation on fault surfaces "A" and "C." The traces of Fault Segments "A," "C" (solid white lines), and "b" (dashed white line) are displayed on the observation surface. Significant along-strike displacement gradients developed at the border of the overstep region. See Figure S6 in the supporting information for a color-blind adapted version of this figure section. (b) Kinematic "irregularities" of the VCFZ. Detail of the kinematic map in Figure 9 focused on the central sector of the VCFZ, which is characterized by a kinematic decoupling between the fault core and breccia units. The plots display poles to slip vectors of faults reported in the map (black poles) and smaller scale ones (red poles). Due to the reactivation of inherited lateral ramps, extensional fault slip vectors within the BU show scattered directions from NNE to SSW, while those related to the master and secondary faults within the fault core (CU1 + CU2) are pointing toward SW.

three dimensions. In particular, the slip tendency analysis allowed us to determine the likelihood (i.e., ratio of resolved shear stress [τ] to effective normal stress [σ'_n]) of the single fault surfaces to slide due to their attitude under a uniform far-field stress (Morris et al., 1996; Figure 13). On the other hand, the elastic model considered the effect of slip accumulation along two right-stepping segments of the VCFZ master fault ("A" and "C") on footwall subsidiary fault surfaces (Figure 14).

The slip tendency analysis was performed with MOVE on the 3-D fault network model of the VCFZ. We computed a normalized slip tendency (NTs), ranging between 0 and 1, by assuming that the maximum slip tendency value was reached when the resolved shear stress equaled the failure shear stress in the Mohr space (Figure 13). Using this assumption, the slip tendency only depends on (i) the orientation of the fault surfaces with respect to the principal stresses, (ii) the stress shape ratio, and (iii) the coefficient of friction (Bistacchi et al., 2012; Collettini & Trippetta, 2007; Lisle & Srivastava, 2004; see the supporting information). We used the principal stress orientations (σ1 N292/85 − σ2 N139/04 − σ3 N48/02) and shape ratio ($\varphi = 0.56$) derived by Ferrarrini et al. (2015) by inverting the focal mechanisms of the 2009 L'Aquila seismic sequence, which are coherent with the NE-SW extension active in the region. A typical coefficient of friction (μ) of 0.6 and a cohesion of 5 MPa were assumed as realistic values for fractured carbonates (e.g., Carpenter et al., 2016). Under these assumptions, the maximum values of normalized slip tendency (NTs > 0.9) within the VCFZ network were obtained for NW-SE striking fault surfaces, both SW and NE dipping with angles of 60–80°, which are abundant within the central overstepping region (Segment "b"; Figures 13a and 13b). Synthetic and antithetic fault surfaces striking WNW-ESE with dip angles >45° showed NTs 0.7-0-9 increasing with dip angle, while synthetic fault surfaces with dip angles <45° (i.e., inverted frontal ramps) showed NTs values of 0.5–0.7. Oblique N-S to NE-SW striking fault surfaces, which are severely misoriented with respect to the applied stress field, showed values of NTs < 0.4. This is the case of inherited lateral ramps

and tear faults within the VCFZ (see Figures 7, 13a, and 13b). The geometric incompatibility of these structures is still persistent if we consider their activation according to a re-shearing criterion (i.e., no cohesion), differently from the newly formed NW-SE striking faults (Figure 13c). The unique possibility to activate these misoriented structures under the resolved applied far-field stress is to consider them as "weak" faults ($\mu \leq 0.3$, e.g., Bolognesi & Bistacchi, 2018) (Figure 13c). Even if this option cannot be excluded for some of the major thrust planes of the Gran Sasso thrust system, which may be associated to weak and continuous phyllosilicates-rich layers, the lateral ramps mapped in the field were entirely developed within a strong dolomitic protolith.

We therefore consider an alternative scenario in which the activation of the inherited N-S to NE-SW striking faults is associated to local stress field perturbations produced at the overstep region during the long-term progressive (i.e., interseismic) to sudden (i.e., coseismic) slip accumulation along the two WNW-ESE striking segments, "A" and "C," of the VCFZ master fault (Figures 12 and 14). We used a 3-D elastic model to infer displacements on Faults "A" and "C" as they are loaded with a far-field stress. The orientation of the principal stress axes and the shape ratio of the stress tensor are the same used for the slip tendency analysis. The magnitude of the principal stress axes was constrained by estimating the confining pressure active at 2 km depth (i.e., estimated VCFZ exhumation depth) in fractured carbonate rocks, without pore pressure. We used the Fault Response Modelling (FRM) module of MOVE: a BEM code based on elastic dislocation theory (i.e., only linear-elastic deformation is assumed, with no brittle or plastic behavior). The FRM uses triangular dislocation elements to model fault-related deformation in an elastic half-space, where fault surfaces are allowed to slide without friction in response to the applied stress field (e.g., Maerten et al., 2005; Meade, 2007; see the supporting information). According to linear elastic fracture mechanics, an isolated circular "penny-shaped" fault will develop an elliptical slip distribution, but more complicated patterns can arise in a fault network with more realistic geometries (e.g., merging or intersecting faults; Jeyakumaran et al., 1992). The input geometry in our simplified model are the 3-D Fault Surfaces "A" and "C," representing the two main segments of the VCFZ master fault (Figure 14), which are right-stepped subparallel with no significant overlap. As a consequence, the on-fault slip distribution along the two surfaces is virtually independent. Starting from the 3-D fault network model in Figure 10, we further extended the Fault Surfaces "A" and "C" in the vertical direction ($\pm$300 m from the topography level) to cover all the elastic space occupied by the subsidiary fault surfaces in the footwall. The mechanical response in the elastic half-space due to slip on the two fault segments was calculated on an observation surface in terms of total displacement (Figure 14a) or displacement along N-S, E-W, and vertical directions (see Figures S7 and S8 in the supporting information). Under the applied far-field stress, the Fault Surfaces "A" and "C" accommodated extension with maximum slip up to 0.7 m and a small right-lateral component (Figure 14a). As an effect of the master fault segmentation and the modeled elliptical slip distribution for each fault surface, maxima of displacement occur in the central portion of the fault segments, while minima occur in the overstep region. This implies the development of significant along-strike displacement gradients at the border of the overstep region, which can be accommodated by preexisting N-S to NE-SW striking faults (Figure 14b). This modeled scenario can be considered as a snapshot during the lateral propagation and early mechanical interaction of the Fault Segments "A" and "C" (prior to their linkage), which are highly compatible with the oblique reactivation of transverse inherited structures (Figures 14a and 14b). This setting is very consistent with the kinematic decoupling described in the overstep region between the faults of core units (CU1-2) and the BU (Figure 14b). Our inferences are also in agreement with previous studies based on detailed BEM models of relay zones with various geometry and degree of mechanical interaction, which indicate the buildup of high Coulomb shear stresses within the relay zones favoring development of secondary faults and linkage of master fault segments (Crider, 2001; Crider & Pollard, 1998). The BEM elastic model presented here is meant to conceptualize, for the scope of the discussion, a single but exemplar moment during the development of the VCFZ master fault. A more complete BEM, testing a simplified geometry of the 3-D VCFZ network with full mechanical interaction between master and subsidiary fault surfaces and local stress field calculations will be treated in a dedicated study.

9.3. Inferences on the Down-dip Structure and Mechanics of the VCFZ

The VCFZ belongs to the larger CIFS, which is considered seismically active based on paleoseismological investigations (e.g., Galadini et al., 2003). In addition, the exhumed VCFZ footwall block also contains

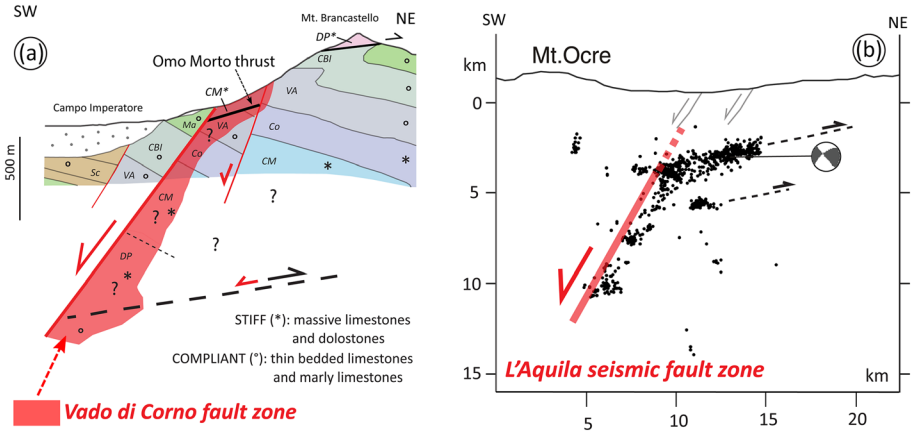

Figure 15. The VCFZ seismic source analog. (a) Conceptual scheme of possible downdip segmentation and thickness variation of the VCFZ. Thickness variations of the VCFZ might be controlled by the mechanical interaction between the extensional fault zone and inherited thrust zones both near the surface (the OMTZ) and at depth (other splay of the Gran Sasso thrust system). The interaction between extensional and compressional features can produce geometrical asperities also due to the tectonic juxtaposition of rock layer with significantly different elastic properties. Lithologies from older to younger: *DP = Dolomia Principale, CM = Calcare Massiccio, Co = Corniola, VA = Verde Ammonitico, CBI = Calcari Bioclastici Inferiori, Ma = Maiolica, Sc = Scaglia.* (b) Local view of the across-strike geometry of the L'Aquila seismic fault zone as illuminated by the aftershock the 2009 L'Aquila seismic sequence (modified after Valoroso et al., 2013). The aftershocks distribution illuminates a flat-like geometry at depth of 2–4 km that is segmented downdip into a higher angle (dip angle ~60°) fault, which is interpreted as the main fault ruptured during the 2009 L'Aquila seismic sequence. Moreover, both the geometry and thickness of the aftershocks zone are varying with depth. Qualitatively, this large-scale geometry, suggesting the superposition of normal seismic faulting on inherited compressional structures, can be nicely compared with the structure of the VCFZ mapped in the Campo Imperatore area.

structural features, from the mesoscale to the microscale, suggesting the propagation of multiple earthquake ruptures at depth (Demurtas et al., 2016). These evidences are mainly concentrated within the fault core cataclastic units (CU1 and CU2) and the high-strain damage zone (HSDZ) which are characterized by in situ shattered fault rocks and discrete fault slip zones with extreme shear strain localization (Figure 6; Demurtas et al., 2016). These slip zones display potential evidence of crystal-plastic deformation mechanisms and fluid pressurization during fast coseismic slip propagation (e.g., mirror-like slip surfaces sharply truncating dolostone clasts, intensely sheared calcite veins with calcite grains foam-like texture, and cataclastites and utracataclasites with "fluidization textures"; Demurtas et al., 2019; De Paola et al., 2015; Fondriest et al., 2013; Siman-Tov et al., 2013, 2015; Smeraglia et al., 2017; Smith et al., 2013, 2017; Passelegue et al., 2019).

The mapped segments of the VCFZ master fault are expected to merge into a single, larger one at depth. The exposure of the VCFZ indicates a minimum (the external limit of the damage zone was not mapped) fault zone footwall thickness of 300–400 m, in the hanging wall of the OMTZ (Figure 5). The exposed fault zone is dominated by intensely fractured carbonates and is characterized by a large-scale (kilometric) downdip geometrical and kinematic asperity due to the interaction of the extensional VCFZ and the older OMTZ. The occurrence of the thrust zone, associated with fault-related dolomitization, produced a further mechanical asperity by putting in contact stiff partially dolomitized Lower to Middle Jurassic platform carbonates in the hanging wall (*Calcare Massiccio*), with more compliant thin-bedded Middle Jurassic to Paleogene basinal and marly limestones (*Verde Ammonitico* to *Scaglia*, see Figure 1) in the footwall block (Figure 15). This setting could be associated with significant variations of the VCFZ thickness and deformation style moving from the hanging wall (e.g., intense fracturing) to the footwall (e.g., fault-related folding and intense dissolution) of the OMTZ with depth. According to this conceptual scheme, even if a general thinning of the VCFZ with depth is expected due to increasing confining pressure, local down-dip fault zone thickening might occur where the extensional VCFZ cuts through and interacts with deeper splays of the Gran Sasso thrust system, due to the buildup of stress concentrations (Figure 15a). In addition, the juxtaposition of units with different elastic properties both in conformable stratigraphic sequence (i.e., mechanical stratigraphy effect)

or in tectonic contact (e.g., previous thrust faults) is expected to significantly influence the fault zone development (e.g., fault propagation, slip accumulation, and off-fault deformation) both in quasi-static and dynamic scenarios (e.g., Aben et al., 2016; Ben-Zion & Shi, 2005; Cappa et al., 2014; Dor et al., 2006; Manighetti et al., 2004). Despite the lack of solid constraints (i.e., fault exposures at deeper structural levels and drilling data) in support of this structural template, the occurrence of active seismic sources with similar geometries has been revealed by recent seismicity in the Central Apennines (e.g., Chiaraluce et al., 2011, 2017; Improta et al., 2019). In particular, the M_w 6.1 L'Aquila 2009 mainshock, which ruptured the L'Aquila extensional seismic fault, was characterized by an aftershock sequence illuminating both the geometry of the extensional master fault zone and a low-angle structure in the footwall block between the depths of 2 and 4 km hosted within a carbonate succession equivalent to that cut by the VCFZ (Demurtas et al., 2016; Valoroso et al., 2013). The low-angle structure has been interpreted as the flat of an older thrust (likely the Gran Sasso thrust), which has been involved in the extensional faulting (Chiaraluce et al., 2011; Demurtas et al., 2016; Falcucci et al., 2015). The few available focal mechanisms do not reveal if extensional faulting implied a reactivation of the thrust flat rather than the activation of synthetic higher angle small extensional faults in the hanging wall block (Chiaraluce et al., 2011). The aftershock cloud illuminating the low-angle structure and the intersection area with the L'Aquila master fault is up to 1 km thick, whereas aftershocks are more localized along the extensional L'Aquila seismic fault at depth (Figure 15b; Valoroso et al., 2013). Similarly, during the 2016 Amatrice-Visso-Norcia seismic sequence, an inherited thrust fault (the Mts. Sibillini Thrust) was observed to control the segmentation of the seismic extensional faults and to act both as barrier and asperity during two distinct, but temporally closed, mainshocks (Improta et al., 2019). Following this line of thought, the along-strike and downdip geometrical and mechanical heterogeneities produced by the interaction of seismogenic normal fault zones with older thrust zones, coupled with the effect of mechanical stratigraphy, could be one of the main factors controlling the spatiotemporal evolution of the seismic sequences striking this area of the Apennines and the highly heterogeneous coseismic slip and rupture velocity distributions modeled for many of the moderate to large in magnitude earthquakes ($M_w \geq 6$) striking the region (e.g., Chiaraluce et al., 2017; Cirella et al., 2012; Improta et al., 2019).

10. Conclusions

We quantified the internal structure of a ~2 km long segment of the VCFZ, an extensional seismically active fault zone cutting through carbonate host rocks in the Central Apennines of Italy. We produced a high-resolution structural map of the VCFZ footwall block with the aim of describing the three-dimensional lateral complexity of both master and subsidiary fault surfaces and the spatial arrangement of the different structural units (i.e., fault zone rocks) encompassing both the fault core and damage zone. Starting from the map, a three-dimensional fault network (fault mesh) model was built, by integrating structural data collected on the surface such as (i) fault surface geometry and topology, (ii) fault kinematics, and (iii) fault rock distribution. The combination of the map and the three-dimensional fault network allowed us to (i) determine the thickness and spatial relations of the different fault rock units, (ii) analyze the three-dimensional kinematic framework of the whole fault zone, and (iii) quantify the topology of the fault network. As a relevant outcome, we were able to reconstruct in 3-D the articulated geometry of a pre-existing thrust zone (OMTZ; Ghisetti & Vezzani, 1991; Demurtas et al., 2016), which is cut and partially inverted by the extensional fault zone. The combination of the (i) high-resolution structural map, (ii) 3-D fault network model, and (iii) kinematic and topological analyses pointed out the crucial role that the older thrust zone geometry (i.e., the occurrence and position of the lateral ramps) played in controlling the along-strike segmentation and kinematic irregularities of the extensional VCFZ. These results were discussed in the framework of regional extension with a slip tendency analysis and a simplified BEM elastic model in three dimensions, which highlight the relevance of misoriented inherited faults in controlling the distributions and partitioning of slip during the lateral propagation of the VCFZ segments.

The exhumed VCFZ represents a good analog of the shallow portion of active seismogenic sources in the Central Apennines. Based on our study, the mechanical interaction of the inherited OMTZ and the extensional VCFZ, generated along-strike and down-dip geometrical and mechanical asperities. Similar structural features might represent main controlling factors of (i) the complex spatio-temporal evolution of seismic sequence striking the Central Apennines and (ii) the highly heterogeneous coseismic slip and rupture

velocity distributions characterizing several mainshocks in the region (e.g., 2009 M_w 6.1 L'Aquila earthquake).

Data Availability Statement

The data supporting this work are publicly available online, DOI: 10.6084/m9.figshare.12578684 (https://figshare.com/s/7a583487d204fbe0302d).

Acknowledgments

The authors warmly thank the "Ente Parco Nazionale del Gran Sasso e Monti della Laga" for allowing to conduct field work in the Campo Imperatore area and the Regione Abruzzo for providing the aerial photographs. We thank Petroleum Expert Ltd./Midland Valley Exploration for providing MOVE through their Academic Initiative. The Gocad Research Group and Paradigm Geophysical are acknowledged for welcoming Milano-Bicocca University into the Gocad Consortium and providing SKUA-GOCAD. Ashley Stanton Yonge is thanked for fruitful discussions. The authors thank the Associate Editor Michele Cooke, Jack Williams, and two anonymous reviewers for their constructive and helpful comments, which significantly contribute to improve the manuscript. This research was funded by the European Research Council Consolidator Grant Project (NOFEAR) 614705 (M. F., M. D., and G. D. T.), M.F. acknowledge the MSCA-IF DAMAGE 839880 for financial support.

References

Aben, F. M., Doan, M.-L., Mitchell, T. M., Toussaint, R., Reuschle, T., Fondriest, M., et al. (2016). Dynamic fracturing by successive coseismic loadings leads to pulverization in active fault zones. *Journal of Geophysical Research: Solid Earth*, *121*, 2338–2360. https://doi.org/10.1002/2015JB012542

Adamoli, L., Calamita, F., & Pizzi, A. (2012). Note Illustrative del Foglio 349 "G. Sasso" della Carta Geologica d'Italia alla scala 1: 50.000. ISPRA, Roma.

Agosta, F., & Kirschner, D. (2003). Fluid conduits in carbonate-hosted seismogenicnormal faults of central Italy. *Journal of Geophysical Research*, *108*(B4), 2221. https://doi.org/10.1029/2002JB002013

Amoroso, O., Russo, G., De Landro, G., Zollo, A., Garambois, S., Mazzoli, S., et al. (2017). From velocity and attenuation tomography to rock physical modeling: Inferences on fluid-driven earthquake processes at the Irpinia fault system in southern Italy. *Journal of Geophysical Research: Letters*, *44*, 6752–6760. https://doi.org/10.1002/2016GL072346

Balsamo, F., Clemenzi, L., Storti, F., Mozafari, M., Solum, J., Swennen, R., et al. (2016). Anatomy and paleofluid evolution of laterally-restricted extensional fault zones in the Jabal Qusaybah anticline, Salakh Arc, Oman. *Geological Society of America Bulletin*, *128*(5-6), 957–972. https://doi.org/10.1130/B31317.1

Barton, C. C., & Hsieh, P. A. (1989). *Physical and hydrologic-flow properties of fractures. Field Trip Guideb* (Vol. T385). Washington D.C: AGU.

Ben-Zion, Y. (1998). Properties of seismic fault zone waves and their utility for imaging low-velocity structures. *Journal of Geophysical Research*, *103*(B6), 12,567–12,585. https://doi.org/10.1029/98JB00768

Ben-Zion, Y., & Shi, Z. (2005). Dynamic rupture on a material interface with spontaneous generation of plastic strain in the bulk. *Earth and Planetary Science Letters*, *236*(1-2), 486–496. https://doi.org/10.1016/j.epsl.2005.03.025

Bistacchi, A., Massironi, M., & Menegon, L. (2010). Three-dimensional characterization of a crustal-scale fault zone: The Pusteria and Sprechenstein fault system (Eastern Alps). *Journal of Structural Geology*, *32*(12), 2022–2041. https://doi.org/10.1016/j.jsg.2010.06.003

Bistacchi, A., Massironi, M., Menegon, L., Bolognesi, F., & Donghi, V. (2012). On the nucleation of non-andersonian faults along phyllosilicate-rich mylonite belts. *Geological Society of London, Special Publication*, *367*(1), 185–199. https://doi.org/10.1144/SP367.13

Boccaletti, M., Elter, P., & Guazzone, G. (1971). Plate tectonic models for the development of the western Alps and northern Apennines. *Nature*, *234*(49), 108–111.

Bolognesi, F., & Bistacchi, A. (2018). A km-scale "triaxial experiment" reveals the extreme mechanical weakness and anisotropy of mica-schists (Grandes Rousses Massif, France). *Journal of Structural Geology*, *107*(July 2017), 53–63. https://doi.org/10.1016/j.jsg.2017.12.001

Caine, J. S., Evans, J. P., & Forster, C. B. (1996). Fault zone architecture and permeability structure. *Geology*, *24*(11), 1025–1028. https://doi.org/10.1130/0091-7613(1996)024<1025:FZAAPS>2.3.CO;2

Calamita, F., Pelorosso, M., & Satolli, S. (2003). The role of the Adria Mesozoic paleomargin architecture on the Gran Sasso d'Italia orogenic system (Central Apennines). *Bollettino della Società Geologica Italiana*, *122*, 337–349.

Cappa, F., Perrin, C., Manighetti, I., & Delor, E. (2014). Off-fault long-term damage: A condition to account for generic, triangular earthquake slip profiles. *Geochemistry, Geophysics, Geosystems*, *15*(4), 1476–1493. https://doi.org/10.1002/2013GC005182

Cardello, G., & Doglioni, C. (2014). From Mesozoic rifting to Apennine orogeny: The gran Sasso range (Italy). *Gondwana Research*, *27*(4), 1307–1334. https://doi.org/10.1016/j.gr.2014.09.009

Carpenter, B. M., Collettini, C., Viti, C., & Cavallo, A. (2016). The influence of normal stress and sliding velocity on the frictional behaviour of calcite at room temperature: Insights from laboratory experiments and microstructural observations. *Geophysical Journal International*, *205*(1), 548–561. https://doi.org/10.1093/gji/ggw038

Caumon, G., Antoine, C., & Tertois, A.-L. (2007). Building 3D geological surfaces from field data using implicit surfaces. Proceedings of the 27th Gocad Meeting, 6

Chester, F. M., Evans, J. P., & Biegel, R. L. (1993). Internal structure and weakening mechanisms of the San-Andreas Fault. *Journal of Geophysical Research*, *98*(B1), 771–786. https://doi.org/10.1029/92JB01866

Chester, F. M., & Logan, J. M. (1987). Composite planar fabric of gouge from Punchbowl Fault, California. *Journal of Structural Geology*, *9*(5-6), 621–IN6. https://doi.org/10.1016/0191-8141(87)90147-7

Chiarabba, C., Amato, A., Anselmi, M., Baccheschi, P., Bianchi, I., Cattaneo, M., et al. (2009). The 2009 L'Aquila (central Italy) M_w 6.3 earthquake: Main shock and aftershocks. *Geophysical Research Letters*, *36*, L18308. https://doi.org/10.1029/2009GL039627

Chiaraluce, L., Di Stefano, R., Tinti, E., Scognamiglio, L., Michele, M., Casarotti, E., et al. (2017). The 2016 central Italy seismic sequence: A first look at the mainshocks, aftershocks, and source models. *Seismological Research Letters*, *88*(3), 757–771. https://doi.org/10.1785/0220160221

Chiaraluce, L., Valoroso, L., Piccinini, D., Di Stefano, R., & De Gori, P. (2011). The anatomy of the 2009 L'Aquila normal fault system (central Italy) imaged by high resolution foreshock and aftershock locations. *Journal of Geophysical Research*, *116*, B12311. https://doi.org/10.1029/2011JB008352

Cirella, A., Piatanesi, A., Tinti, E., Chini, M., & Cocco, M. (2012). Complexity of the rupture process during the 2009 L'Aquila, Italy, earthquake. *Geophysical Journal International*, *190*(1), 607–621. https://doi.org/10.1111/j.1365-246X.2012.05505.x

Clemenzi, L., Storti, F., Balsamo, F., Molli, G., Ellam, R., Muchez, P., & Swennen, R. (2015). Fluid pressure cycles, variations in permeability, and weakening mechanisms along low-angle normal faults: The Tellaro detachment, Italy. *Geological Society of America Bullettin*, *127*(11–12), 1689–1710. https://doi.org/10.1130/B31203.1

Cochran, E. S., Li, Y. G., Shearer, P. M., Barbot, S., Fialko, Y., & Vidale, J. E. (2009). Seismic and geodetic evidence for extensive, long-lived fault damage zones. *Geology*, *37*(4), 315–318. https://doi.org/10.1130/G25306A.1

Collanega, L., Jackson, C. A. L., Bell, R. E., Coleman, A. J., Lenhart, A., & Breda, A. (2019). Normal fault growth influenced by basement fabrics: The importance of preferential nucleation from pre-existing structures. *Basin Research*, *31*(4), 659–687. https://doi.org/10.1111/bre.12327

Collettini, C., & Trippetta, F. (2007). A slip tendency analysis to test mechanical and structural control on aftershock rupture planes. *Earth and Planetary Science Letters*, *255*(3-4), 402–413. https://doi.org/10.1016/j.epsl.2007.01.001

Crider, J. G. (2001). Oblique slip and the geometry of normal-fault linkage: Mechanics and a case study from the basin and range in Oregon. *Journal of Structural Geology*, *23*(12), 1997–2009. https://doi.org/10.1016/S0191-8141(01)00047-5

Crider, J. G., & Pollard, D. D. (1998). Fault linkage: Three-dimensional mechanical interaction between echelon normal faults. *Journal of Geophysical Research*, *103*(B10), 24,373–24,391. https://doi.org/10.1029/98JB01353

D'Agostino, N., Avallone, A., Cheloni, D., D'anastasio, E., Mantenuto, S., & Selvaggi, G. (2008). Active tectonics of the Adriatic region from GPS and earthquake slip vectors. *Journal of Geophysical Research*, *113*, B12413. https://doi.org/10.1029/2008JB005860

D'Agostino, N., Chamot-Rooke, N., Funiciello, R., Jolivet, L., & Speranza, F. (1998). The role of pre-existing thrust faults and topography on the styles of extension in the Gran Sasso range (central Italy). *Tectonophysics*, *292*(3-4), 229–254. https://doi.org/10.1016/S0040-1951(98)00070-5

De Paola, N., Holdworth, R. E., Viti, C., Collettini, C., & Bullock, R. (2015). Can grain size sensitive flow lubricate faults during the initial stages of earthquake propagation? *Earth and Planetary Science Letters*, *431*, 48–58. https://doi.org/10.1016/j.epsl.2015.09.002

Delogkos, E., Manzocchi, T., Childs, C., Camanni, G., & Roche, V. (2020). The 3D structure of a normal fault from multiple outcrop observations. *Journal of Structural Geology*, *136*, 104009. https://doi.org/10.1016/j.jsg.2020.104009

Demurtas, M., Fondriest, M., Balsamo, F., Clemenzi, L., Storti, F., Bistacchi, A., & Di Toro, G. (2016). Structure of a normal seismogenic fault zone in carbonates: The Vado di Corno Fault, Campo Imperatore, Central Apennines (Italy). *Journal of Structural Geology*, *90*, 185–206. https://doi.org/10.1016/j.jsg.2016.08.004

Demurtas, M., Smith, S. A. F., Prior, D. J., Brenker, F. E., & Di Toro, G. (2019). Grain size sensitive creep during simulated seismic slip in nanogranular fault gouges: Constraints from transmission Kikuchi diffraction (TKD). *Journal of Geophysical Research: Solid Earth*, *124*, 10,197–10,209. https://doi.org/10.1029/2019JB018071

Dershowitz, W. S., & Herda, H. H. (1992). Interpretation of fracture spacing and intensity. In J. R. Tillerson, & W. R. Wawersik (Eds.), *Proceedings of the 33rd U.S. Symposium on rock mechanics* (pp. 757–766). Santa Fe, New Mexico: Balkema, Rotterdam.

Di Stefano, R., Chiarabba, C., Chiaraluce, L., Cocco, M., De Gori, P., Piccinini, D., & Valoroso, L. (2011). Fault zone properties affecting the rupture evolution of the 2009 (M_w 6.1) L'Aquila earthquake (central Italy): Insights from seismic tomography. *Geophysical Research Letters*, *38*, L10310. https://doi.org/10.1029/2011GL047365

Di Toro, G., & Pennacchioni, G. (2005). Fault plane processes and mesoscopic structure of a strong-type seismogenic fault in tonalites (Adamello batholith, Southern Alps). *Tectonophysics*, *402*(1–4), 55–80. https://doi.org/10.1016/j.tecto.2004.12.036

Dor, O., Ben-Zion, Y., Rockwell, T. K., & Brune, J. (2006). Dynamic rupture on a material interface with spontaneous generation of plastic strain in the bulk. *Earth and Planetary Science Letters*, *245*(3-4), 642–654. https://doi.org/10.1016/j.epsl.2006.03.034

Elter, P., Giglia, G., Tongiorni, M., & Trevisan, L. (1975). Tensional and compressional areas in recent (Tortonian to present) evolution of Northern Apennines. *Bollettino di Geofisica Teorica e Applicata*, *42*, 3–18.

Fagereng, Å., & Sibson, R. H. (2010). Melange rheology and seismic style. *Geology*, *38*(8), 751–754. https://doi.org/10.1130/G30868.1

Falcucci, E., Gori, S., Moro, M., Fubelli, G., Saroli, M., Chiarabba, C., & Galadini, F. (2015). Deep reaching versus vertically restricted Quaternary normal faults: Implications on seismic potential assessment in tectonically active regions: Lessons from the middle Aterno valley fault system, central Italy. *Tectonophysics*, *651-652*, 186–198. https://doi.org/10.1016/j.tecto.2015.03.021

Faulkner, D., Jackson, C., Lunn, R., Schlische, R., Shipton, Z., Wibberley, C., & Withjack, M. (2010). A review of recent development concerning the structure, mechanics and fluid flow properties of fault zones. *Journal of Structural Geology*, *32*(11), 1557–1575. https://doi.org/10.1016/j.jsg.2010.06.009

Faulkner, D. R., Lewis, A. C., & Rutter, E. H. (2003). On the internal structure and mechanics of large strike-slip fault zones: Field observations of the Carboneras fault in southeastern Spain. *Tectonophysics*, *367*(3-4), 235–251. https://doi.org/10.1016/S0040-1951(03)00134-3

Ferrarrini, F., De Nardis, R., Lavecchia, G., & Brozzetti, F. (2015). Fault geometry and active stress from earthquakes and field geology data analysis: The Colfiorito 1997 and L'Aquila 2009 cases (Central Italy). *Pure and Applied Geophysics*, *172*(5), 1079–1103. https://doi.org/10.1007/s00024-014-0931-7

Fondriest, M., Aretusini, S., Di Toro, G., & Smith, S. A. F. (2015). Fracturing and rock pulverization along an exhumed seismogenic fault zone in dolostones: The Foiana Fault Zone (Southern Alps, Italy). *Tectonophysics*, *654*, 56–74. https://doi.org/10.1016/j.tecto.2015.04.015

Fondriest, M., Doan, M.-L., Aben, F., Fusseis, F., Mitchell, T. M., Voorn, M., et al. (2017). Static versus dynamic fracturing in shallow carbonate fault zones. *Earth and Planetary Science Letters*, *461*, 8–19. https://doi.org/10.1016/j.epsl.2016.12.024

Fondriest, M., Smith, S. A. F., Candela, T., Nielsen, S., Mair, K., & Di Toro, G. (2013). Mirror-like faults and power dissipation during earthquakes. *Geology*, *41*(11), 1175–1178. https://doi.org/10.1130/G34641.1

Fondriest, M., Smith, S. A. F., Di Toro, G., Zampieri, D., & Mittempergher, S. (2012). Fault zone structure and seismic slip localization in dolostones, an example from the Southern Alps, Italy. *Journal of Structural Geology*, *45*, 52–67. https://doi.org/10.1016/j.jsg.2012.06.014

Galadini, F., Galli, P., & Moro, M. (2003). Paleoseismology of silent faults in the Central Apennines (Italy): The Campo Imperatore Fault (gran Sasso range fault system). *Annals of Geophysics*, *46*(5), 793–813.

Galli, P., Galadini, F., Moro, M., & Giraudi, C. (2002). New paleoseismological data from the Gran Sasso d'Italia area (Central Apennines). *Geophysical Research Letters*, *29*(7), 1134. https://doi.org/10.1029/2001GL013292

Ghisetti, F., & Vezzani, L. (1990). *Carta Geologica del Gran Sasso d'Italia (da Vado di Corno a Passo delle Capannelle)*. Florence, Italy: S.EL.CA.

Ghisetti, F., & Vezzani, L. (1991). Thrust belt development in the Central Apennines (Italy): Northward polarity of thrusting and out-of-sequence deformations in the Gran Sasso Chain. *Tectonics*, *10*(5), 904–919. https://doi.org/10.1029/91TC00902

Giraudi, C., & Frezzotti, M. (1995). Palaeoseismicity in the Gran Sasso Massif (Abruzzo, Central Italy). *Quaternary International*, *25*, 81–93. https://doi.org/10.1016/1040-6182(94)P3716-L

Giraudi, C., & Frezzotti, M. (1997). Late Pleistocene glacial events in the Central Apennines, Italy. *Quaternary Research*, *48*(3), 280–290. https://doi.org/10.1006/qres.1997.1928

Hale, D. (2013). Methods to compute fault images, extract fault surfaces, and estimate fault throws from 3D seismic images. *Geophysics*, *78*(2), O33–O43. https://doi.org/10.1190/geo2012-0331.1

Hollinsworth, A. D., Koehn, D., Dempster, T. J., & Aanyu, K. (2019). Structural controls on the interaction between basin fluids and a rift flank fault: Constraints from the Bwamba Fault, East African Rift. *Journal of Structural Geology*, *118*, 236–249. https://doi.org/10.1016/j.jsg.2018.10.012

Iacopini, D., Butler, R. W. H., Purves, S., McArdle, N., & De Freslon, N. (2016). Exploring the seismic expression of fault zones in 3D seismic volumes. *Journal of Structural Geology*, *89*, 54–73. https://doi.org/10.1016/j.jsg.2016.05.005

Improta, L., Latorre, D., Margheriti, L., Nardi, A., Marchetti, A., Lombardi, A. M., et al. (2019). Multi-segment rupture of the 2016 Amatrice-Visso-Norcia seismic sequence (central Italy) constrained by the first high-quality catalog of early aftershocks. *Scientific Reports*, *9*, 1–13.

Ispra (2012). Carta Geologica d'Italia, sheet 349 "Gran Sasso d'Italia". APAT, Servizio Geologico d'Italia. S.EL.CA, Florence, Italy

Jeyakumaran, M., Rudnicki, J. W., & Keer, L. M. (1992). Modeling slip zones with triangular dislocation elements. *Bulletin of Seismological Society of America*, *82*, 2153–2169.

Jolivet, L., & Faccenna, C. (2000). Mediterranean extension and the Africa-Eurasia collision. *Tectonics*, *19*(6), 1095–1106. https://doi.org/10.1029/2000TC900018

Jolivet, L., Faccenna, C., Goffe, B., Mattei, M., Rossetti, F., Brunet, C., et al. (1998). Midcrustal shear zones in postorogenic extension: Example from the northern Tyrrhenian Sea. *Journal of Geophysical Research*, *103*(B6), 12,123–12,160. https://doi.org/10.1029/97JB03616

Kirkpatrick, J. D., Bezerra, F. H. R., Shipton, Z. K., Do Nascimento, A. F., Pytharouli, S. I., Lunn, R. J., & Soden, A. M. (2013). Scale-dependent influence of pre-existing basement shear zones on rift faulting: A case study from NE Brazil. *Journal of the Geological Society*, *170*(2), 237–247. https://doi.org/10.1144/jgs2012-043

Kolawole, F., Atekwana, E. A., Lao-Davila, D. A., Abdelsalam, M. G., Chindandali, P. R., Salima, J., & Kalindekafe, L. (2018). Active deformation of Malawi rift's north basin Hinge zone modulated by reactivation of preexisting Precambrian Shear zone fabric. *Tectonics*, *37*, 683–704. https://doi.org/10.1002/2017TC004628

Lavecchia, G., Brozzetti, F., Barchi, M., Menichetti, M., & Keller, J. V. A. (1994). Seismotectonic zoning in east-central Italy deduced from an analysis of the Neogene to present deformations and related stress fields. *Geological Society of America Bullettin*, *106*(9), 1107–1120. https://doi.org/10.1130/0016-7606(1994)106<1107:SZIECI>2.3.CO;2

Leah, H., Fondriest, M., Lucca, A., Storti, F., Balsamo, F., & Di Toro, G. (2018). Coseismic extension recorded within the damage zone of the Vado di Ferruccio Thrust Fault, Central Apennines, Italy. *Journal of Structural Geology*, *114*, 121–138. https://doi.org/10.1016/j.jsg.2018.06.015

Lisle, R. J., & Srivastava, D. C. (2004). Test of the frictional reactivation theory for faults and validity of fault-slip analysis. *Geology*, *32*(7), 569. https://doi.org/10.1130/G20408.1

Lucca, A., Storti, F., Balsamo, F., Clemenzi, L., Fondriest, M., Burgess, R., & Di Toro, G. (2019). From submarine to subaerial out-of-sequence thrusting and gravity-driven extensional faulting: Gran Sasso Massif, Central Apennines, Italy. *Tectonics*, *38*, 4155–4184. https://doi.org/10.1029/2019TC005783

Maerten, F., Resor, P., Pollard, D., & Maerten, L. (2005). Inverting for slip on three-dimensional fault surfaces using angular dislocations. *Bulletin of Seismological Society of America*, *95*(5), 1654–1665. https://doi.org/10.1785/0120030181

Malinverno, A., & Ryan, W. B. (1986). Extension in the Tyrrhenian Sea and shortening in the Apennines as result of arc migration driven by sinking of the lithosphere. *Tectonics*, *5*(2), 227–245. https://doi.org/10.1029/TC005i002p00227

Manighetti, I., King, G., & Sammin, C. G. (2004). The role of off-fault damage in the evolution of normal faults. *Earth and Planetary Science Letters*, *217*(3-4), 399–408. https://doi.org/10.1016/S0012-821X(03)00601-0

Manzocchi, T. (2002). The connectivity of two-dimensional networks of spatially correlated fractures. *Water Resources Research*, *38*(9), 1162. https://doi.org/10.1029/2000WR000180

Marrett, R., & Allmendinger, R. W. (1990). Kinematic analysis of fault-slip data. *Journal of Structural Geology*, *12*(8), 973–986. https://doi.org/10.1016/0191-8141(90)90093-E

Masoch, S., Fondriest, M., Preto, N., Secco, M., & Di Toro, G. (2019). Seismic cycle recorded in cockade-bearing faults (Col de Teghime, Alpine Corsica). *Journal of Structural Geology*, *129*, 103889. https://doi.org/10.1016/j.jsg.2019.103889

Mayolle, S., Soliva, R., Caniven, Y., Wibberley, C., Ballas, G., Milesi, G., & Dominguez, S. (2019). Scaling of fault damage zones in carbonate rocks. *Journal of Structural Geology*, *124*, 35–50. https://doi.org/10.1016/j.jsg.2019.03.007

Meade, B. J. (2007). Algorithms for the calculation of the exact displacements, strains, and stresses for triangular dislocation elements in a uniform elastic half space. *Computer & Geosciences*, *33*(8), 1064–1075. https://doi.org/10.1016/j.cageo.2006.12.003

Morris, A., Ferrill, D. A., & Henderson, D. B. (1996). Slip-tendency analysis and fault reactivation. *Geology*, *24*(3), 275–278. https://doi.org/10.1130/0091-7613(1996)024<0275:STAAFR>2.3.CO;2

Mort, K., & Woodcock, N. H. (2008). Quantifying fault breccia geometry: Dent fault, NW England. *Journal of Structural Geology*, *30*(6), 701–709. https://doi.org/10.1016/j.jsg.2008.02.005

Nyberg, B., Nixon, C. W., & Sanderson, D. J. (2018). NetworkGT: A GIS tool for geometric and topological analysis of two-dimensional fracture networks. *Geosphere*, *14*(4), 1618–1634. https://doi.org/10.1130/GES01595.1

Ortega, O., & Marrett, R. (2000). Prediction of macrofracture properties using microfracture information, Mesaverde Group sandstones, San Juan basin, New Mexico. *Journal of Structural Geology*, *22*(5), 571–588. https://doi.org/10.1016/S0191-8141(99)00186-8

Parotto, M., & Praturlon, A. (1975). Geological summary of the Central Apennines. *Quaderni della Ricerca Scientifica*, *90*, 257–300.

Passelegue, F. X., Aubry, J., Nicolas, A., Fondriest, M., Deldicque, D., Schubnel, A., & Di Toro, G. (2019). From fault creep to slow and fast earthquakes in carbonates. *Geology*, *47*(8), 744–748. https://doi.org/10.1130/G45868.1

Patacca, E., Sartori, R., & Scandone, P. (1990). Tyrrhenian basin and Apenninic arcs: Kinematic relations since late Tortonian times. *Memorie della Societa Geologica Italiana*, *45*(1), 425–451.

Patacca, E., Scandone, P., Di Luzio, E., Cavinato, G. P., & Parotto, M. (2008). Structural architecture of the central Apennines: Interpretation of the CROP 11 seismic profile from the Adriatic coast to the orographic divide. *Tectonics*, *27*, TC3006. https://doi.org/10.1029/2005TC001917

Petit, J.-P. (1987). Criteria for the sense of movement on fault surfaces in brittle rocks. *Journal of Structural Geology*, *9*(5-6), 597–608. https://doi.org/10.1016/0191-8141(87)90145-3

Petit, J. P., Proust, F., & Tapponnier, P. (1983). Critères du sens du mouvement sur les miroirs de failles en roches non calcaires. *Bulletin de la Société géologique de France*, *7*, 589–608.

Philips, T. B., Jackson, C. A., Bell, R. E., Duffy, O. B., & Fossen, H. (2016). Reactivation of intrabasement structures during rifting: A case study from offshore southern Norway. *Journal of Structural Geology*, *91*, 54–73. https://doi.org/10.1016/j.jsg.2016.08.008

Phillips, T. B., Fazlikhani, H., Gawthorpe, R. L., Fossen, H., Jackson, C. A.-L., Bell, R. E., et al. (2019). The influence of structural inheritance and multiphase extension on rift development, the northern North Sea. *Tectonics*, *38*, 4099–4126. https://doi.org/10.1029/2019TC005756

Pischiutta, M., Fondriest, M., Demurtas, M., Magnoni, F., Di Toro, G., & Rovelli, A. (2017). Structural control on the directional amplification of seismic noise (Campo Imperatore, central Italy). *Earth and Planetary Science Letters*, *471*, 10–18. https://doi.org/10.1016/j.epsl.2017.04.017

Pizzi, A., Di Domenica, A., Gallovič, F., Luzi, L., & Puglia, R. (2017). Fault segmentation as constraint to the occurrence of the main shocks of the 2016 Central Italy seismic sequence. *Tectonics*, *36*, 2370–2387. https://doi.org/10.1002/2017TC004652

Ross, Z. E., Cochran, E. S., Trugman, D. T., & Smith, J. D. (2020). 3D fault architecture controls the dynamism of earthquake swarms. *Science*, *368*(6497), 1357–1361. https://doi.org/10.1126/science.abb0779

Rowe, C. D., & Griffith, W. A. (2015). Do faults preserve a record of seismic slip: A second opinion. *Journal of Structural Geology*, *78*, 1–26. https://doi.org/10.1016/j.jsg.2015.06.006

Santantonio, M., & Carminati, E. (2011). Jurassic rifting evolution of the Apennines and Southern Alps (Italy): Parallels and differences. *Geological Society of America Bullettin*, *123*(3–4), 468–484. https://doi.org/10.1130/B30104.1

Serpelloni, E., Anzidei, M., Baldi, P., Casula, G., & Galvani, A. (2005). Crustal velocity and strain-rate fields in Italy and surrounding regions: New results from the analysis of permanent and non-permanent GPS networks. *Geophysical Journal International*, *161*(3), 861–880. https://doi.org/10.1111/j.1365-246X.2005.02618.x

Sibson, R. H. (1977). Fault rocks and fault mechanisms. *Journal of the Geological Society*, *133*(3), 191–213. https://doi.org/10.1144/gsjgs.133.3.0191

Sibson, R. H. (1986). Earthquakes and rock deformation in crustal fault zones. *Annual Reviews in Planetary Sciences*, *14*(1), 149–175. https://doi.org/10.1146/annurev.ea.14.050186.001053

Siman-Tov, S., Aharanov, E., Sagy, A., & Emmanuel, S. (2013). Nanograins form carbonate fault mirrors. *Geology*, *41*(6), 703–706. https://doi.org/10.1130/G34087.1

Siman-Tov, S., Aharonov, E., Boneh, Y., & Reches, Z. E. (2015). Fault mirrors along carbonate faults: Formation and destruction during shear experiments. *Earth Planet. Science Letters*, *430*, 367–376.

Smeraglia, L., Billi, A., Carminati, E., Cavallo, A., & Doglioni, C. (2017). Field-to nano-scale evidence for weakening mechanisms along the fault of the 2016 Amatrice and Norcia earthquakes, Italy. *Tectonophysics*, *712*, 156–169.

Smith, S. A. F., Billi, A., Di Toro, G., & Spiess, R. (2011). Principal slip zones in limestone: Microstructural characterization and implications for the seismic cycle (Tre Monti fault, Central Apennines, Italy). *Pure and Applied Geophysics*, *168*(12), 2365–2393. https://doi.org/10.1007/s00024-011-0267-5

Smith, S. A. F., Bistacchi, A., Mitchell, T. M., Mittempergher, S., & Di Toro, G. (2013). The structure of an exhumed intraplate seismogenic fault in crystalline basement. *Tectonophysics*, *599*, 2944.

Smith, S. A. F., Di Toro, G., Kim, S., Ree, J.-H., Nielsen, S., Billi, A., & Spiess, R. (2013). Coseismic recrystallization during shallow earthquake slip. *Geology*, *41*(1), 63–66. https://doi.org/10.1130/G33588.1

Smith, S.A.F., Griffiths, J.R., Fondriest, M., & Di Toro, G. (2017). "Coseismic foliations" in Gouge and cataclasite: Experimental observations and consequences for interpreting the fault rock record. Fault zone dynamic processes: Evolution of fault properties during seismic rupture, AGU Monograph Series, 81–102

Snoke, A. W., Tullis, J., & Todd, V. R. (1998). *Fault-related rocks: A photographic atlas*. Chichester, Wesr Sussex: Princeton University Press.

Speranza, F., Tavarnelli, E., Calamita, F., & Paltrinieri, W. (2003). Passive-margin heritage on thrust-system development: Evidence from Corno Grande (Gran Sasso range, Italy). *Bollettino della Società Geologica Italiana*, *122*, 233–249.

Speranza, F., & Minelli, L. (2014). Ultra-thick Triassic dolomites control the rupture behavior of the central Apennine seismicity: Evidence from magnetic modeling of the L'Aquila fault zone. *Journal of Geophysical Research: Solid Earth*, *119*, 6756–6770. https://doi.org/10.1002/2014JB011199

Storti, F., Balsamo, F., Mozafari, M., Koopman, A., Swennen, R., & Taberner, C. (2018). Syn-contractional overprinting between extension and shortening along the Montagna dei Fiori Fault during Plio-Pleistocene antiformal stacking at the Central Apennines thrust wedge toe. *Tectonics*, Special volume geodynamics, crustal and lithospheric tectonics, and active deformation in the Mediterranean regions. A tribute to Prof Renato Funiciello, *37*(10), 3690–3720. https://doi.org/10.1029/2018TC005072

Storti, F., Billi, A., & Salvini, F. (2003). Particle size distributions in natural carbonate fault rocks: Insights for non-self-similar cataclasis. *Earth and Planetary Science Letters*, *206*(1-2), 173–186. https://doi.org/10.1016/S0012-821X(02)01077-4

Swanson, M. T. (1988). Pseudotachylyte-bearing strike-slip duplex structures in the fort Foster brittle zone, S. Maine. *Journal of Strucutral Geology*, *10*(8), 813–828. https://doi.org/10.1016/0191-8141(88)90097-1

Tesei, T., Collettini, C., Viti, C., & Barchi, M. (2013). Fault architecture and deformation mechanisms in exhumed analogues of seismogenic carbonate-bearing thrusts. *Journal of Structural Geology*, *55*, 167–181. https://doi.org/10.1016/j.jsg.2013.07.007

Valoroso, L., Chiaraluce, L., Piccinini, D., Stefano, R., Schaff, D., & Waldhauser, F. (2013). Radiography of a normal fault system by 64,000 high-precision earthquake locations: The 2009 L'Aquila (central Italy) case study. *Journal of Geophysical Research*, *118*, 1156–1176. https://doi.org/10.1002/jgrb.50130

Vezzani, L., Festa, A., & Ghisetti, F. C. (2010). Geology and tectonic evolution of the central-southern Apennines, Italy. *Geological Society of America Special Papers*, *469*, 1–58.

Vidale, J. E., & Li, Y.-G. (2003). Damage to the shallow Landers fault from the nearby Hector mine earthquake. *Nature*, *421*(6922), 524–526. https://doi.org/10.1038/nature01354

Wibberley, C. A., Yielding, G., & Di Toro, G. (2008). Recent advances in the understanding of fault zone internal structure: A review. *Geological Society of London Special Publications*, *299*(1), 5–33. https://doi.org/10.1144/SP299.2

Williams, J. N., Fagereng, Å., Wedmore, L. N., Biggs, J., Mphepo, F., Dulanya, Z., et al. (2019). How do variably striking faults reactivate during rifting? Insights from southern Malawi. *Geochemistry, Geophysics, Geosystems*, *20*, 3588–3607. https://doi.org/10.1029/2019GC008219